Investigation of the 240Pu(n, f) reaction at the n_TOF/EAR2 facility in the 9 meV–6 MeV range

(n_TOF Collaboration) Stamatopoulos, A.; Tsinganis, A.; Colonna, N.; Kokkoris, M.; Vlastou, R.; Diakaki, M.; Žugec, P.; Schillebeeckx, P.; Gunsing, F.; Sabaté-Gilarte, M.; ...

Repository / Repozitorij:

Repository of the Faculty of Science - University of Zagreb

Investigation of the ^{240}Pu(n, f) reaction at the n_TOF/EAR2 facility in the 9 meV–6 MeV range

A. Stamatopoulos[1,*] A. Tsinganis,[1,2] N. Colonna,[3] M. Kokkoris,[1] R. Vlastou,[1] M. Diakaki,[4,1] P. Žugec,[5] P. Schillebeeckx,[6]
F. Gunsing,[4,2] M. Sabaté-Gilarte,[2,7] M. Barbagallo,[3] O. Aberle,[2] J. Andrzejewski,[8] L. Audouin,[9] V. Bécares,[10] M. Bacak,[11]
J. Balibrea,[10] S. Barros,[12] F. Bečvář,[13] C. Beinrucker,[14] F. Belloni,[4] E. Berthoumieux,[4] J. Billowes,[15] D. Bosnar,[5] M. Brugger,[2]
M. Caamaño,[16] S. Lo Meo,[17,18] F. Calviño,[19] M. Calviani,[2] D. Cano-Ott,[10] F. Cerutti,[2] E. Chiaveri,[2] G. Cortés,[19]
M. A. Cortés-Giraldo,[7] L. Cosentino,[20] L. A. Damone,[3,21] K. Deo,[22] C. Domingo-Pardo,[23] R. Dressler,[24] E. Dupont,[4]
I. Durán,[16] B. Fernández-Domínguez,[16] A. Ferrari,[2] P. Ferreira,[12] P. Finocchiaro,[20] R. J. W. Frost,[15] V. Furman,[25] K. Göbel,[14]
A. R. García,[10] I. Gheorghe,[26] T. Glodariu,[26,†] I. F. Gonçalves,[12] E. González-Romero,[10] A. Goverdovski,[27] E. Griesmayer,[11]
C. Guerrero,[7] H. Harada,[28] T. Heftrich,[14] S. Heinitz,[24] A. Hernández-Prieto,[2,19] J. Heyse,[6] D. G. Jenkins,[29] E. Jericha,[11]
F. Käppeler,[30] Y. Kadi,[2] T. Katabuchi,[31] P. Kavrigin,[11] V. Ketlerov,[27] V. Khryachkov,[27] A. Kimura,[28] N. Kivel,[24] I. Knapova,[13]
M. Krtička,[13] E. Leal-Cidoncha,[16] C. Lederer,[14,32] H. Leeb,[11] J. Lerendegui-Marco,[7] M. Licata,[18,33] R. Losito,[2] D. Macina,[2]
J. Marganiec,[8] T. Martínez,[10] C. Massimi,[18,33] P. Mastinu,[34] M. Mastromarco,[3] F. Matteucci,[35,36] E. Mendoza,[10] A. Mengoni,[17]
P. M. Milazzo,[35] F. Mingrone,[18] M. Mirea,[26] S. Montesano,[2] A. Musumarra,[20,37] R. Nolte,[38] F. R. Palomo-Pinto,[7]
C. Paradela,[16] N. Patronis,[39] A. Pavlik,[40] J. Perkowski,[8] A. Plompen,[6] J. I. Porras,[2,41] J. Praena,[7] J. M. Quesada,[7]
T. Rauscher,[42,43] R. Reifarth,[14] A. Riego-Perez,[19] M. Robles,[16] C. Rubbia,[2] J. A. Ryan,[15] A. Saxena,[22] S. Schmidt,[14]
D. Schumann,[24] P. Sedyshev,[25] A. G. Smith,[15] S. V. Suryanarayana,[22] G. Tagliente,[3] J. L. Tain,[23] A. Tarifeño-Saldivia,[23]
L. Tassan-Got,[9] S. Valenta,[13] G. Vannini,[18,33] V. Variale,[3] P. Vaz,[12] A. Ventura,[18] V. Vlachoudis,[2] A. Wallner,[44] S. Warren,[15]
M. Weigand,[14] C. Weiss,[2,11] and T. Wright[15]

(n_TOF Collaboration)

[1]*National Technical University of Athens, Athens, Greece*
[2]*European Organization for Nuclear Research (CERN), Geneva, Switzerland*
[3]*Istituto Nazionale di Fisica Nucleare, Sezione di Bari, Bari, Italy*
[4]*CEA Irfu, Université Paris-Saclay, F-91191 Gif-sur-Yvette, France*
[5]*Department of Physics, Faculty of Science, University of Zagreb, Zagreb, Croatia*
[6]*European Commission, Joint Research Centre, Retieseweg 111, B-2440 Geel, Belgium*
[7]*Universidad de Sevilla, Sevilla, Spain*
[8]*University of Lodz, Lodz, Poland*
[9]*Institut de Physique Nucléaire, CNRS-IN2P3, Université Paris-Sud, Université Paris-Saclay, F-91406 Orsay Cedex, France*
[10]*Centro de Investigaciones Energéticas Medioambientales y Tecnológicas (CIEMAT), Madrid, Spain*
[11]*Technische Universität Wien, Wien, Austria*
[12]*Instituto Superior Técnico, Lisbon, Portugal*
[13]*Charles University, Prague, Czech Republic*
[14]*Goethe University, Frankfurt, Germany*
[15]*University of Manchester, Manchester, United Kingdom*
[16]*University of Santiago de Compostela, Santiago de Compostela, Spain*
[17]*Agenzia Nazionale per le Nuove Tecnologie (ENEA), Bologna, Italy*
[18]*Istituto Nazionale di Fisica Nucleare, Sezione di Bologna, Bologna, Italy*
[19]*Universitat Politècnica de Catalunya, Barcelona, Spain*
[20]*INFN Laboratori Nazionali del Sud, Catania, Italy*
[21]*Dipartimento di Fisica, Università degli Studi di Bari, Bari, Italy*
[22]*Bhabha Atomic Research Centre (BARC), Mumbai, India*
[23]*Instituto de Física Corpuscular, CSIC - Universidad de Valencia, Valencia, Spain*
[24]*Paul Scherrer Institut (PSI), Villingen, Switzerland*
[25]*Joint Institute for Nuclear Research (JINR), Dubna, Russia*
[26]*Horia Hulubei National Institute of Physics and Nuclear Engineering, Bucharest, Romania*
[27]*Institute of Physics and Power Engineering (IPPE), Obninsk, Russia*
[28]*Japan Atomic Energy Agency (JAEA), Tokai-mura, Japan*
[29]*University of York, York, United Kingdom*
[30]*Karlsruhe Institute of Technology, Campus North, IKP, 76021 Karlsruhe, Germany*
[31]*Tokyo Institute of Technology, Tokyo, Japan*
[32]*School of Physics and Astronomy, University of Edinburgh, Edinburgh, United Kingdom*
[33]*Dipartimento di Fisica e Astronomia, Università di Bologna, Bologna, Italy*
[34]*Istituto Nazionale di Fisica Nucleare, Sezione di Legnaro, Legnaro, Italy*
[35]*Istituto Nazionale di Fisica Nucleare, Sezione di Trieste, Trieste, Italy*

^{36}*Dipartimento di Astronomia, Università di Trieste, Trieste, Italy*

^{37}*Dipartimento di Fisica e Astronomia, Università di Catania, Catania, Italy*

^{38}*Physikalisch-Technische Bundesanstalt (PTB), Bundesallee 100, 38116 Braunschweig, Germany*

^{39}*University of Ioannina, Ioannina, Greece*

^{40}*University of Vienna, Faculty of Physics, Vienna, Austria*

^{41}*University of Granada, Granada, Spain*

^{42}*Centre for Astrophysics Research, University of Hertfordshire, Hatfield, United Kingdom*

^{43}*Department of Physics, University of Basel, Basel, Switzerland*

^{44}*Australian National University, Canberra, Australia*

Background: Nuclear waste management is considered amongst the major challenges in the field of nuclear energy. A possible means of addressing this issue is waste transmutation in advanced nuclear systems, whose operation requires a fast neutron spectrum. In this regard, the accurate knowledge of neutron-induced reaction cross sections of several (minor) actinide isotopes is essential for design optimization and improvement of safety margins of such systems. One such case is ^{240}Pu, due to its accumulation in spent nuclear fuel of thermal reactors and its usage in fast reactor fuel. The measurement of the ^{240}Pu(n, f) cross section was previously attempted at the CERN n_TOF facility EAR1 measuring station using the time-of-flight technique. Due to the low amount of available material and the given flux at EAR1, the measurement had to last several months to achieve a sufficient statistical accuracy. This long duration led to detector deterioration due to the prolonged exposure to the high α activity of the fission foils, therefore the measurement could not be successfully completed.

Purpose: It is aimed to determine whether it is feasible to study neutron-induced fission at n_TOF/EAR2 and provide data on the ^{240}Pu(n, f) reaction in energy regions requested for applications.

Methods: The study of the ^{240}Pu(n, f) reaction was made at a new experimental area (EAR2) with a shorter flight path which delivered on average 30 times higher flux at fast neutron energies. This enabled the measurement to be performed much faster, thus limiting the exposure of the detectors to the intrinsic activity of the fission foils. The experimental setup was based on microbulk Micromegas detectors and the time-of-flight data were analyzed with an optimized pulse-shape analysis algorithm. Special attention was dedicated to the estimation of the non-negligible counting loss corrections with the development of a new methodology, and other corrections were estimated via Monte Carlo simulations of the experimental setup.

Results: This new measurement of the ^{240}Pu(n, f) cross section yielded data from 9 meV up to 6 MeV incident neutron energy and fission resonance kernels were extracted up to 10 keV.

Conclusions: Neutron-induced fission of high activity samples can be successfully studied at the n_TOF/EAR2 facility at CERN covering a wide range of neutron energies, from thermal to a few MeV.

I. INTRODUCTION

A. Motivation

A significant fraction of electricity production (25% in Europe [1]) is based on nuclear sources; however, this results in the accumulation of long-lived radioactive waste. A possible means of disposing this waste is through its transmutation in advanced nuclear systems, such as Gen-IV reactors [2,3] and accelerator driven systems [4,5], which will be operated with a fast neutron spectrum. The consumption of known uranium resources by 2050 [6] should also be considered in the design of future power plants since it constrains the

nuclear fuel possibilities. The accurate knowledge of neutron-induced reactions is therefore essential for feasibility studies and optimum operation of such systems. At the same time, the improvement of safety margins of thermal reactors which are currently in operation is considered equally important, therefore the accurate knowledge of cross sections on fertile isotopes is also required. In this respect, the Nuclear Energy Agency (NEA) [7] has introduced the High Priority Request List (HPRL) [8] in which data on a plethora of reactions and derived quantities are requested.

^{240}Pu(n, f) is among these reactions since 2008 [9] and up to present the requested accuracies [10] have not been met. ^{240}Pu is a long-lived fertile plutonium isotope and is produced in conventional reactors from neutron capture on ^{239}Pu, therefore it plays an important role in the U/Pu cycle affecting the breeding process. In addition, about $\approx$60 kg of ^{240}Pu are annually discharged per reactor unit [11], which is a significant quantity to be used as fuel in future fast reactors.

Finally, the intermediate structures that can be observed in the (n, f) cross section in the resolved resonance region can provide constraints on phenomenological fission models

---

*athanasios.stamatopoulos@cern.ch

†Deceased.

through the characterization of resonance properties. At the same time, resonance structures appear in the cross section in the hundreds of keV region near the threshold fission, as an effect of vibrational states in the second well of the double-humped fission barrier, which require a combination of high flux and resolution to be observed and can contribute to the understanding of the fission mechanism.

B. Previous measurements

Due to the importance of the ^{240}Pu(n, f) reaction, many data sets exist in the EXFOR database [12] covering incident neutron energies from 25.3 meV up to 200 MeV. More specifically, the cross section was measured at the thermal point by Pratt *et al.* ($\sigma_{\text{th}} = 3700(8000)$ mb, [13]) and Eastwood *et al.* ($\sigma_{\text{th}} = 30(45)$ mb, [14]), and both results were uncertain and discrepant by more than two orders of magnitude. In addition, spectrum and Maxwellian average cross section at the thermal point were reported by Bigham [15] and Hulet *et al.* [16], respectively.

The first resonance in the ^{240}Pu $+ n$ system is observed 1.05 eV above the neutron separation energy. For neutron-induced fission, only a single data set exists in this region, reported by Leonard *et al.* [17], which was obtained with poor neutron energy resolution.

Up to 5 keV, several measurements have been performed; however only the data by Weston *et al.* [18] have the level of resolution and statistics required to perform resonance analyses, according to the extensive argumentation of Bouland *et al.* [19].

Between 5 and 50 keV, the data reported by Weston [18] and by Budtz-Jorgensen and Knitter [20] show overlapping class-II resonance structures which are quite discrepant. For instance the structures seen at $E_n \approx 13.5$ keV (Fig. 19) and 20 keV are discrepant by 40% and 30%, respectively.

Above 50 keV up to the vicinity of the fission threshold, a plethora of measurements has been performed. The three latest ones were reported by Salvador-Castineira *et al.* [21], Tovesson *et al.* [22], and Laptev *et al.* [23] and discrepancies that reach up to 15% were observed. In addition, the latest time-of-flight data by Tovesson *et al.* [22] are of insufficient resolution to observe structures attributed to vibrational phenomena.

Finally, in the first chance fission plateau up to 6 MeV, several measurements have been performed as well. Concerning the three latest ones, the data by Tovesson *et al.* [22] are systematically higher by about 6% compared to the corresponding ones by Salvador-Castineira *et al.* [21] and Laptev *et al.* [23], which justifies the need for additional measurements in this region as well.

C. The need for a second experimental area at n_TOF

A study of the ^{240}Pu(n, f) reaction was attempted at n_TOF in 2010 at the horizontal 185-m-long flight path, commonly referred to as EAR1, using the time-of-flight technique to determine the incident neutron energy [24] and Micromegas fission fragment detectors. The moderate neutron flux delivered at EAR1, inevitably led to a lengthy measurement to

achieve sufficient statistical accuracy in the MeV region. The detectors were therefore exposed for several months to the high intrinsic α activity of the samples, which caused them to deteriorate and eventually rendered the study incomplete.

To further expand the measuring capabilities of n_TOF and to perform studies of important reactions where samples with either high activity, low mass, or small cross section are needed, a second experimental beam line (EAR2) was commissioned in 2014 [25]. The present measurement [26,27], where high activity samples were used, along with the ^{7}Be(n, α) one [28], in which the short half-life of ^{7}Be ($t_{1/2} = 53.2$ d) limits the study of its low cross section, exemplify the capabilities of EAR2, which are a result of the high instantaneous flux and good resolution (see Sec. II A).

Taking advantage of these characteristics, a new study of the ^{240}Pu(n, f) reaction was successfully performed in EAR2. This experimental campaign was the first performed in EAR2 and the derived cross section spanned across nine orders of magnitude in incident neutron energy, ranging from 9 meV up to 6 MeV. The results that will be presented illustrate the potential of EAR2 in completing challenging fission studies, which was also demonstrated by subsequent measurements [29–31].

II. EXPERIMENTAL DETAILS

A. Neutron source

Neutrons at n_TOF are produced by spallation with a 20 GeV/c pulsed proton beam that impinges on a lead block. The spallation target assembly consisted of a cylindrical lead block, 40 cm in length and 60 cm in diameter, which was surrounded by a thin layer of water for cooling and moderation purposes, thus the neutron spectrum delivered in EAR2 covered a broad energy range from thermal energies up to 100 MeV [32].

The proton beam is delivered by CERN's Proton Synchrotron (PS) at a low frequency which does not exceed 0.8 Hz and has a spread of 7 ns RMS. The beam intensity was 6.6×10^{12} protons/bunch on average and was constant within 2%.

The experimental area rests at the end of a 18.4-m-long beamline from the center of the spallation target, which is kept under a 10^{-2} mbar vacuum. The beam was shaped by means of a 3-m-long neutron collimator with an aperture of 2.2 cm, which consisted of 2 m Fe and 1 m polyethylene enriched with boron. The proximity of EAR2 to the target yielded a 30 times higher flux than the one of EAR1, while neutrons needed an approximately 10 times shorter time of flight to reach the experimental area. These attributes resulted in a considerably improved background suppression, as shown in Fig. 1, and mitigated the effects of the strong α activity which occurred in EAR1.

B. Fission foils

Three high purity ^{240}Pu samples in the form of ^{240}PuO$_2$, with a total activity of 19.22 MBq, were originally prepared at EC-JRC-Geel [33] for the measurement in EAR1 but were also used in the EAR2 experimental campaign. The plutonium material was deposited through molecular plating
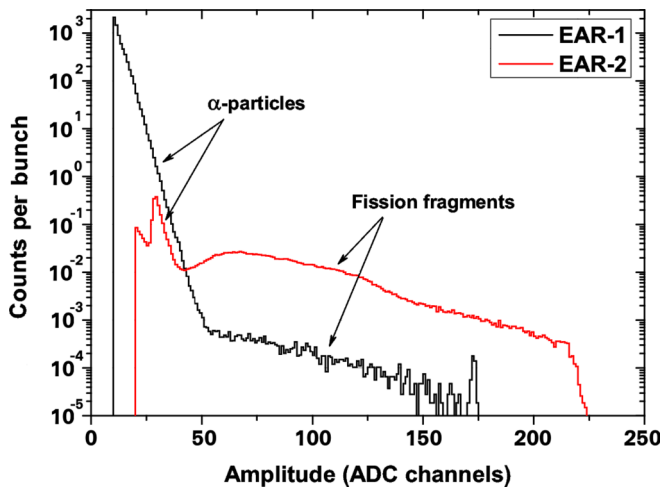
FIG. 1. Amplitude spectra recorded in EAR1 and EAR2 for a ^{240}Pu sample. The α-particle background in EAR2 is appreciably suppressed while the fission rate is significantly higher.

on 0.25-mm-thick and 5-cm-diameter aluminium backings, whereas the deposits themselves had a diameter of 3 cm. It needs to be noted that the small difference in the diameters did not affect the analysis and the results, as shown in Ref. [34].

Two additional samples were used as reference foils: (a) a ^{235}U sample with a 40.5 Bq activity and (b) a ^{238}U sample with 9.4 Bq activity. The ^{235}U deposit had a diameter of 2.9 cm and was in the chemical form of UF$_4$. The ^{238}U sample had a diameter of 3 cm and was made of U(OH)$_6$ material. Both samples were manufactured by means of molecular plating and had aluminium backings similar to the plutonium ones.

The main characteristics of the fission foils used in the measurement can be seen in Table I.

C. Detectors

To detect the fission fragments a setup based on the compact and neutron-transparent microbulk Micromegas detector was used [35]. The gas volume of the detector was divided

in two regions by a thin (5 μm) copper micromesh: (a) the drift region (6 mm), between the cathode and the micromesh and (b) the narrow amplification gap (50 μm) between the micromesh and the 5-μm-thick copper anode. In this configuration, the fission foil was positioned so that the deposit faced the drift region and its backing served as the cathode.

An electric field of the order of 50 kV/cm was applied in the amplification gap, which is sufficient to cause avalanche multiplication resulting in a high detector gain. What is remarkable in this detector is the fact that its gain is intrinsic and depends only on the applied electric field, hence enhancing the ratio of signal to electronic background. This is important in cases where the electronic noise is high and the signal must be individually amplified.

All detector-sample sets were stacked in a cylindrical aluminium chamber which was equipped with 50-μm-thick kapton windows. The spacing between the detector-sample sets was 2 cm. The chamber was filled with a circulating gas mixture of Ar : CF$_4$: iC$_4$H$_{10}$ at 88 : 10 : 2 volume fraction, at atmospheric pressure and room temperature.

The low amount of material present in the Micromegas minimized the production of charged particles from neutron interactions with the detector itself, which was confirmed by an empty cathode-detector set, placed behind the ^{238}U sample, as schematically shown in Fig. 2.

In addition to the fission detectors, a setup based on silicon detectors was used to monitor the neutron beam, based on the detection of α-particles and tritons produced from the ^{6}Li(n, t) reaction. Details on the monitor setup, which is referred to as "SiMon2," can be found in Ref. [36].

D. Data acquisition

Data were digitized through the use of 8-bit flash analog-to-digital converters (ADCs) that were operated at a 500 MHz sampling rate. The acquisition window was 16 ms wide and allowed us to reach down to thermal and cold neutron energies. Finally, an online zero-suppression algorithm was applied to minimize the amount of data recorded during the acquisition [37].

TABLE I. List of the main characteristics of the fission foils used in the experiment along with the estimated uncertainties, provided by JRC-Geel, which were determined in May 2011 for the ^{240}Pu samples, in January 1981 for ^{235}U, and in February 2012 for ^{238}U.

| Sample	Lot	Reference number	Mass (mg)	Areal density (mg/cm^2)	Atomic abundance (%)
^{240}Pu	BC01269B	TP2010-011-01 TP2010-011-03 TP2010-011-04	0.7163(28) 0.809(3) 0.763(3)	0.1017(4) 0.1148(5) 0.1083(5)	^{238}Pu: 0.0733(29) ^{239}Pu: 0.0144(18) ^{240}Pu: 99.8915(18) ^{241}Pu: 0.00041(31) ^{242}Pu: 0.02027(41) ^{244}Pu: 0.000046(88)
Total			2.2883	0.3248	
^{235}U	SP 3576	SP 3576-1	0.563(11)	0.0912(17)	^{234}U: 0.1698 ^{235}U: 99.475 ^{236}U: 0.0273 ^{238}U: 0.3277
^{238}U	2677	TP2011-008-03	0.745(15)	0.1070(22)	^{238}U > 99.9
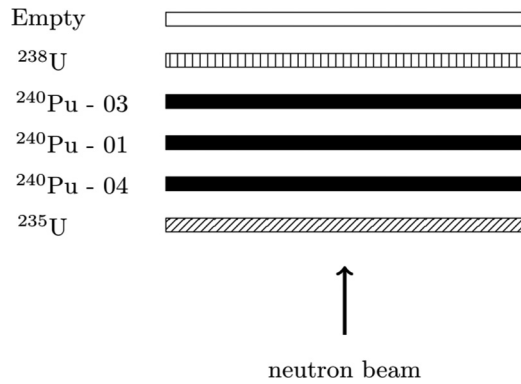
FIG. 2. Schematic view of the fission foil stack, with respect to the neutron beam direction. Apart from the fission samples, an empty cathode was placed to monitor possible proton and α recoils from the detector itself.

## III. DATA REDUCTION AND ANALYSIS

A. Signal processing

The digitized waveforms were processed offline by a pulse shape analysis framework developed at n_TOF [38]. The signal recognition was based on a single-stage differentiation filter whereas the reconstruction of the wave forms was based on pulse shape fitting procedures.

Signal processing was performed in two procedures regarding (a) the so-called γ-flash, which is a burst of photons and relativistic particles that are produced during spallation and arrive promptly at the experimental hall [39], and (b) regular fission and α-particle signals.

a. γ-flash: In the present case, the baseline following the γ-flash had an oscillatory behavior that remained consistent from pulse to pulse. Since fission signals were sitting on the trailing edge of the γ-flash as well as on top of the oscillations, the subtraction of an average γ-flash shape was applied to each individual waveform, as described in detail in Ref. [38].

The calculation of the average shape was achieved from recorded wave forms which were stacked, as shown in Fig. 3. In the calculation, fission signals were not taken into account since they would have distorted the average shape. Such a procedure is important since it can extend to the highest
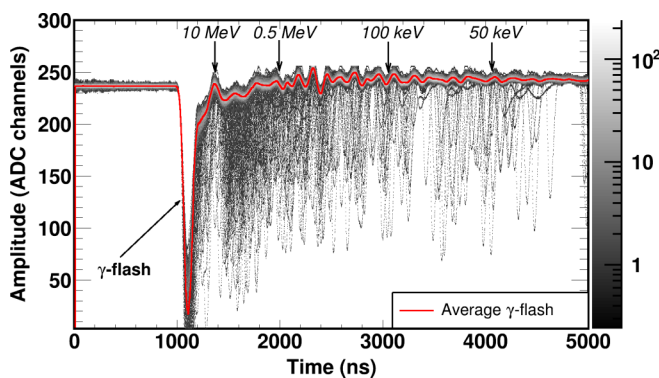

FIG. 3. Stacked recorded waveforms in the γ-flash region for a ^{240}Pu sample. The solid line corresponds to the calculated average. The signals shown correspond to 1% of the statistics. A few indicative neutron energies are also shown.
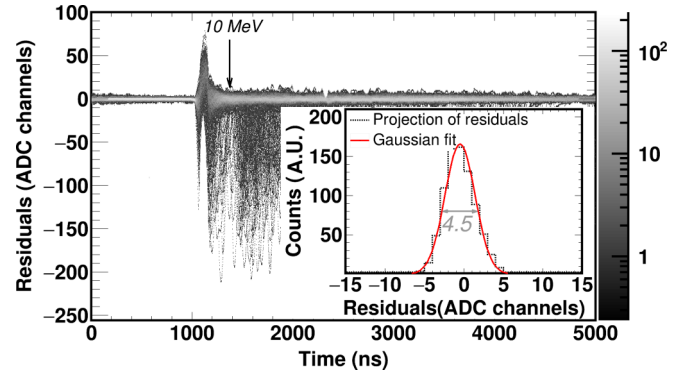
FIG. 4. Stacked residuals between the average γ-flash and the recorded waveforms in the γ-flash region for a ^{240}Pu sample. The inset contains the projection of the residuals to the y axis, up to 10 MeV neutron energy. The signals shown correspond to 1% of the statistics.

reachable neutron energy and it allowed us to better discriminate low-amplitude fission signals that sit on the crest of the oscillations.

This procedure was followed by the calculation of the residuals between the average γ-flash shape and each individual wave form as a means of cross-checking that the subtraction was properly applied and estimating the highest reachable energy. The individual residuals were then stacked and projected along the amplitude axis, as shown in the inset of Fig. 4.

A Gaussian fit on the projected residuals indicated a mean value of 0, which verified that the subtraction was properly applied within an uncertainty of $\approx$5 channels (2% of the full range), up to the time of flight that corresponds to 10 MeV incident neutron energy. For smaller times the projection of the residuals significantly widened, therefore 10 MeV was considered to be the maximum highest reachable energy as far as the signal processing is concerned.

b. Fission signals: A similar approach was followed concerning the fission signals. Isolated detector signals were stacked and average pulse shapes were extracted for each individual detector. These were then fed into the reconstruction routines and pulse shape fitting was applied to determine signal attributes such as the arrival time, the amplitude, etc. This information was then stored in the so-called list mode, in order to perform the offline analysis and reconstruct the reaction yield as a function of the time of flight.

B. Cross section calculation

The cross section was deduced with reference to ^{235}U(n, f) in the regions 9–800 meV and 10 keV–6 MeV, using Eq. (1a). In the 800 meV–10 keV region the evaluated EAR2 flux [32] was used and the cross section was calculated using Eq. (1b):

$$\sigma = \frac{C}{C^{(\mathrm{ref})}} \frac{f_{\mathrm{amp}}}{f_{\mathrm{amp}}^{(\mathrm{ref})}} \frac{f_{\mathrm{imp}}}{f_{\mathrm{imp}}^{(\mathrm{ref})}} \frac{f_{\mathrm{DT}}}{f_{\mathrm{DT}}^{(\mathrm{ref})}} \frac{f_{\mathrm{abs}}}{f_{\mathrm{abs}}^{(\mathrm{ref})}} \frac{f_{\mathrm{shield}}}{f_{\mathrm{shield}}^{(\mathrm{ref})}} \frac{f_{\mathrm{SF}}}{f_{\mathrm{SF}}^{(\mathrm{ref})}} \frac{f_{\gamma f}}{f_{\gamma f}^{(\mathrm{ref})}}$$

$$\times \frac{m^{(\mathrm{ref})}}{m} \frac{\Phi^{(\mathrm{ref})}}{\Phi} \sigma^{(\mathrm{ref})}, \tag{1a}$$

$$\sigma = \frac{C f_{\mathrm{amp}} f_{\mathrm{imp}} f_{\mathrm{DT}} f_{\mathrm{abs}} f_{\mathrm{shield}} f_{\mathrm{SF}} f_{\mathrm{CD}} f_{\gamma f}}{m \Phi}, \tag{1b}$$
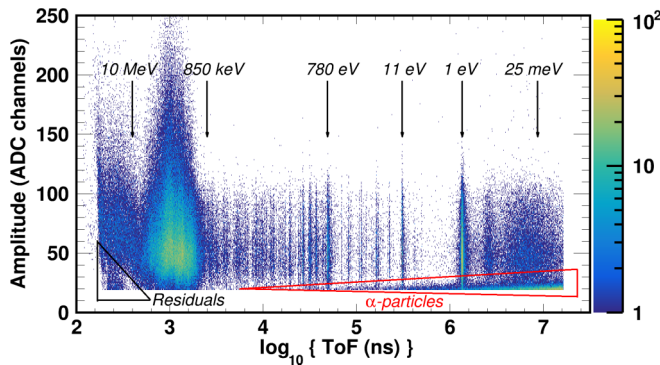
FIG. 5. Typical 2D distribution of the reconstructed time-of-flight and amplitude signals for a ^{240}Pu sample. Residuals from the γ-flash subtraction and signals from the α activity are illustrated in the bottom left and right parts of the figure, respectively. Resonances are also visible. A few indicative neutron energies are shown.

where

(1) C refers to the fission counts.

(2) f_{amp} is the correction factor for the rejected fission signals below the amplitude threshold which was applied to reject α-particles and noise (see Sec. III B 2).

(3) f_{imp} corrects for the parasitic counts that contributed to the recorded yield and were attributed to fission reactions from contaminants or impurities in the fission foils.

(4) f_{DT} is a correction factor applied for counting losses due to dead time, pile-up, and insufficient signal reconstruction effects.

(5) f_{abs} takes into account the self-absorption of fission fragments within the fission foils.

(6) f_{shield} is the correction factor for the neutron self-shielding of the various layers in the detector-sample stacks.

(7) f_{SF} accounts for the contribution of spontaneous fission events.

(8) $f_{\gamma f}$ is the correction factor due to parasitic counts that contributed to the recorded fission yield from photo-fission reactions.

(9) m is the mass term and corresponds to the areal density of the fission foil (Table I).

(10) Φ is the neutron fluence incident at the corresponding foil.

The terms that include the superscript "(ref)" refer to the reference sample.

1. Fission counts

The number of fission events as a function of the time of flight was determined from the signal processing described in Sec. III A. A typical distribution of the reconstructed time of flight vs amplitude can be seen in Fig. 5, for a ^{240}Pu sample. The reconstructed signals were then thoroughly checked in order to reject noise (i.e., saturated signals from sparks in the gas, falsely reconstructed signals, etc.) and to apply the proper thresholds to reject nonfission events (i.e., α-particles). In the
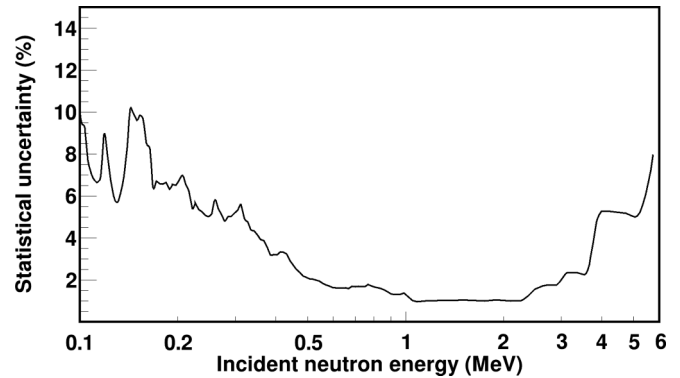

FIG. 6. Statistical uncertainties, after applying the corrections, in the 100 keV–6 MeV high-energy region concerning the lightest ^{240}Pu sample. Up to 1 MeV an isolethargic binning of 100 bins per decade was used whereas in the MeV region a custom binning that is shown in Appendix B was adopted.

latter case the appropriate correction factors were applied to the fission yield, as will be described later in the text.

The statistical uncertainties after the application of the correction factors were of the order of 10% in the thermal region and vary between 6–60% and 5–30% in the resolved and unresolved resonance regions, respectively. These high statistical uncertainties were observed in the valleys between resonances where the reaction rate was quite low. At higher neutron energies the statistical uncertainties did not exceed 8%, as shown in Fig. 6.

2. Amplitude threshold

A typical fission amplitude spectrum, such as the one reconstructed in the present case and shown in Fig. 7, consists mainly of two parts: (a) the fission fragments and (b) the α-particles from the intrinsic radioactivity of the fission foil.
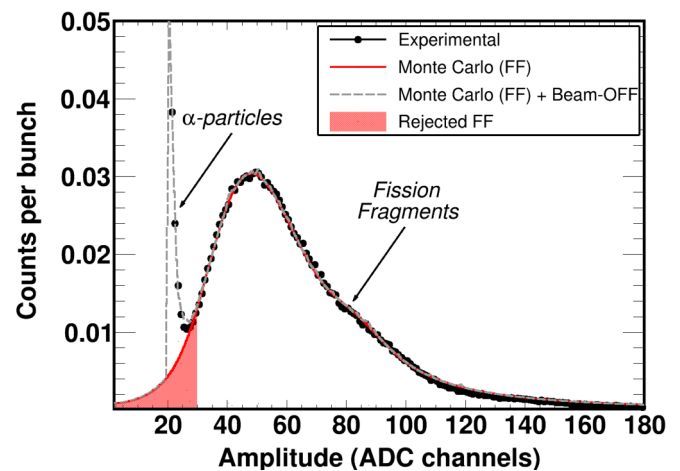

FIG. 7. Comparison between the experimental and simulated amplitude spectra from a ^{240}Pu sample. For the low amplitude region, a beam-off spectrum was added to the simulated one. The reproduction of the experimental points is quite satisfactory. The shaded area represents the fraction of the rejected FF for an amplitude threshold equal to 30 channels.

TABLE II. List of the correction factors that were applied to the fission yields along with the corresponding uncertainties (when estimated). In cases of energy dependent correction factors, a reference to a figure is given. When a single correction factor is given, it corresponds to all fission foils, unless a hyphen is used in the corresponding row.

Sample	f_{amp}	f_{imp}	f_{DT}	f_{abs} (%)	f_{shield}	f_{SF}, f_{CD} (%)	$f_{\gamma f}$ (%)	Φ ratio
^{235}U	1.040(2)	–						1.000
^{240}Pu-04	1.070(4)							0.996
^{240}Pu-01	1.115(10)	Fig. 8	Fig. 10	<0.100(1)	<0.40(2)	<0.2	Fig. 12	0.992
^{240}Pu-03	1.090(9)							0.988
^{238}U	1.020(3)	–						0.984

To reject the α-counts, an amplitude threshold was introduced in the analysis based on beam-off runs to locate the high amplitude tail of the α-particle spectrum. However, a fraction of fission counts was inevitably rejected as well, whose estimation was based on Monte Carlo simulations by coupling the GEF [40] and FLUKA [41] codes.

Fission fragment (FF) distributions were generated in GEF and were then used as a source term in FLUKA. Fission fragments were produced within the sample and propagated towards the gas in order to estimate the deposited energy. The simulated energy deposition was convoluted with an appropriate response function of the detection/read-out system and was finally calibrated in order to be compared to the experimental amplitude spectrum.

The α-particles were not simulated since only a small part of the tailing edge was recorded; however, in order to benchmark the simulations, beam-off spectra, that practically consisted only of α-counts, were used. More specifically, the simulated spectra, which contained only FF, were summed with beam-off amplitude distributions and were then compared to experimental beam-on spectra, which consisted of both FF and α-counts. As characteristically shown for a ^{240}Pu sample in Fig. 7, a quite satisfactory agreement was achieved.

The f_{amp} correction factor can then be estimated from the simulations as the fraction of the integral beneath the corresponding amplitude threshold (shaded area, Fig. 7). The aforementioned procedure was performed individually for the ^{240}Pu, ^{235}U, and ^{238}U samples and correction factors in the 2–11.5% range were determined, as shown in Table II.

To estimate the uncertainty of the simulations, the uranium samples were used. The low activity of these samples (a few tens of Bq) and the narrow acquisition window (16 ms) made the detection of α-particles highly improbable. In this respect, the simulated and experimental fraction of the rejected FF was compared and an agreement within 3% was achieved, which was considered to be the upper bound of systematic uncertainty of this correction factor.

In the simulations, apart from the energy deposition in the gas, several other effects on the correction factor were studied, such as (a) the chemical composition of the samples, which might deviate from the nominal one due to the preparation method [42] and/or environmental conditions (i.e., moisture), and (b) the FF angular distribution which might be important above 1 MeV. In the former case the chemical composition was varied [e.g., in the ^{238}U sample from U(OH)$_6$ to

U(OH)$_{10}$] while in the latter one FF were propagated unidirectionally towards the gas from 0° to 89° with respect to the neutron beam. In both studies the effect on f_{amp} was less than 3% and 1%, respectively. More information can be found in Ref. [34].

3. Impurities

It was previously mentioned that in the ^{240}Pu samples impurities with a total abundance of 0.1% were present (Table I). Despite this small fraction, their contribution to the fission yield was high in the thermal and resolved resonance regions, attributed mainly to the fissile ^{239}Pu. The estimation of the f_{imp} correction factor was based on "weighting" the ENDF/B-VIII.0 evaluated (n, f) cross section $\sigma^{(i)}$ of each isotope found in the samples with its reported atomic abundance $f_{abun}^{(i)}$, as seen in Eq. (2):

$$\sigma_w^{(i)} = f_{abun}^{(i)} \sigma^{(i)}. \tag{2}$$

Then f_{imp} was calculated, pointwise with respect to the neutron energy, from the ratio of Eq. (3), where the sum in the denominator includes the isotopes reported in Table I as
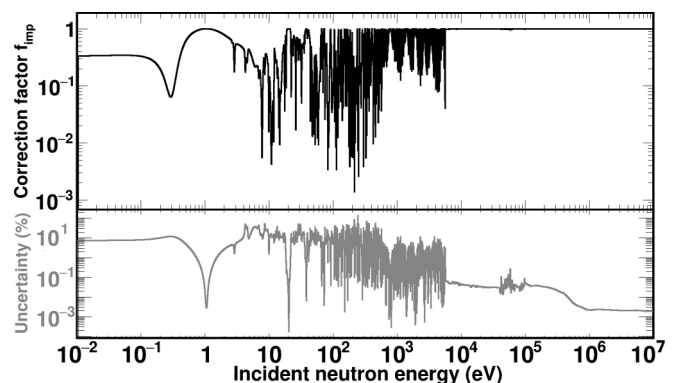

FIG. 8. The f_{imp} correction factor (top panel) applied to ^{240}Pu with respect to the neutron energy. The bottom panel shows the total estimated uncertainty, which was obtained from the diagonal elements of the covariance matrix.

well as the ^{236}U daughter nucleus[1] from the α decay of ^{240}Pu:

$$f_{\text{imp}} = \frac{\sigma_w^{^{240}\text{Pu}}}{\sum_i \sigma_w^{(i)}}; \qquad (3)$$

see also Fig. 8.

The uncertainty in the correction was determined by means of the covariance matrix provided by EC-JRC-Geel. As far as the ENDF/B-VIII.0 cross sections were concerned, the main contribution to the uncertainty was the ^{239}Pu(n, f) cross section, since it was the contaminant that mainly contributed to the fission yield. The ENDF/B-VIII.0 ^{239}Pu(n, f) cross section was evaluated with a 1.4% uncertainty above 2.5 keV, therefore it was considered negligible compared to the uncertainties of the atomic abundances. Below 2.5 keV, the ENDF/B-VIII.0 library reports uncertainties of the order of a few percent ($<4\%$ at a 2 bins/decade binning) which, although non-negligible, was not included in the covariance matrix because its component relies on evaluations which can change in the future; therefore only experimental components were propagated.

In the case of the uranium samples, the corresponding correction was negligible.

4. Counting losses

Below the fission threshold, up to about 1 MeV, the recorded fission rate did not exceed 1 MHz for the plutonium and uranium samples. The analytical correction formulas proposed by Coates [43] and Moore [44] were applied to the recorded fission counts which practically yielded identical corrections. Correction factors less than 0.5% and 25% were estimated in the 9 meV–300 keV and 300 keV–1 MeV regions respectively, concerning ^{240}Pu. For ^{235}U, a 0.6% correction was estimated at 56 meV, where the fission rate peaked in the thermal region. An average 1% correction was applied up to 20 keV while, up to 1 MeV, the estimated counting losses progressively reached 16%. The corresponding correction for ^{238}U was practically negligible.

Above 1 MeV, the expected instantaneous counting rate reached several MHz and resulted in significant pile-up that was observed in the reconstructed counting spectra. Indeed, between 850 keV and 10 MeV (Figs. 3 and 5) signals with systematically higher amplitudes were reconstructed, which is attributed to pile-up effects. The analytical methods used below 1 MeV were not able to provide realistic corrections, therefore a new methodology was developed [45] to treat such cases based on two approaches: (a) exponential decay fits in experimental waiting time distributions as shown in Fig. 9 and (b) correction functions predicted from detector emulation devices. It has to be mentioned that this methodology can also account for an insufficient signal reconstruction, which can occur at high counting rates. It was demonstrated that both approaches provide compatible corrections for counting rates up to 2 MHz; however, the uncertainty of method (a) is higher. In the present measurement, the fission rate in ^{240}Pu was
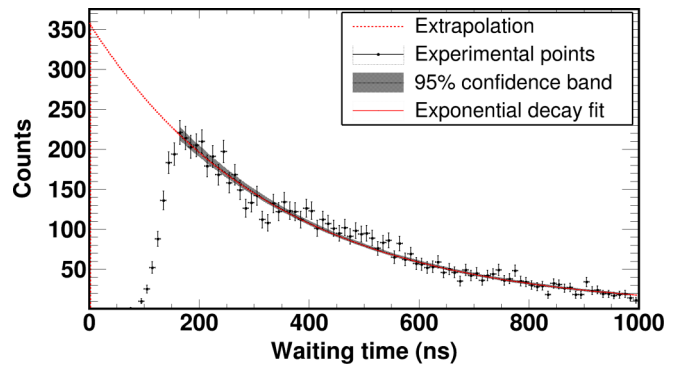
FIG. 9. Exponential fits in waiting time distributions are a useful experimental tool in estimating counting losses by calculating the integral below the extrapolated fitting function [46].

higher than 2 MHz, therefore f_{DT} was estimated by means of fitting waiting time distributions, yielding a correction factor that varied from 1.44 up to 2.26 with 10% uncertainty.

For the uranium samples the correction function described in Ref. [45] was used. The correction factors that were calculated with a 3% uncertainty did not exceed 1.62 and 1.31 for ^{235}U and ^{238}U, respectively. Finally, in Fig. 10 the correction factors are shown that were applied to the recorded fission yield.

It has to be noted that above 6 MeV the waiting time distributions lacked sufficient statistical accuracy, which was a limiting factor for the highest reachable neutron energy. In addition, concerning the 01 and 03 targets, the signal reconstruction above 4 MeV was not possible since the γ-flash subtraction could not be applied at higher energies. In addition, above 3 MeV the trends in the correction factors shown in Fig. 10 are attributed to counting losses not only due to pile-up effects, but also those due to inefficient signal reconstruction.
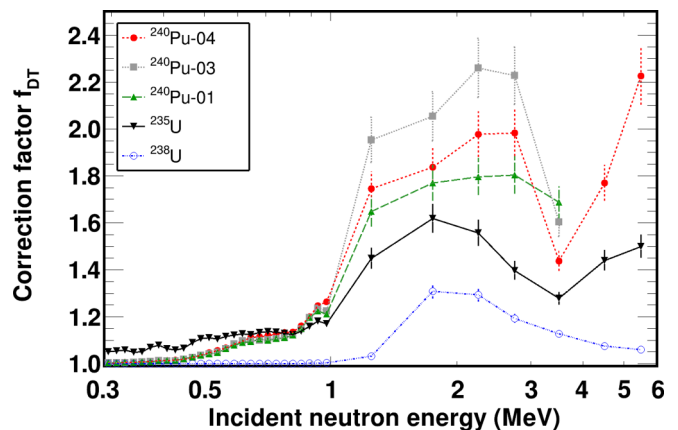
FIG. 10. Estimated correction factors for counting losses. Below 1 MeV the methodology proposed by Coates [43] and Moore [44] was applied, while above 1 MeV the correction was based on Ref. [45]. Average correction factors are shown per 0.5 MeV, above 1 MeV.

---

[1]About 0.04% of the initial ^{240}Pu had decayed to ^{236}U after 3.5 y from the sample characterization when the measurement took place.
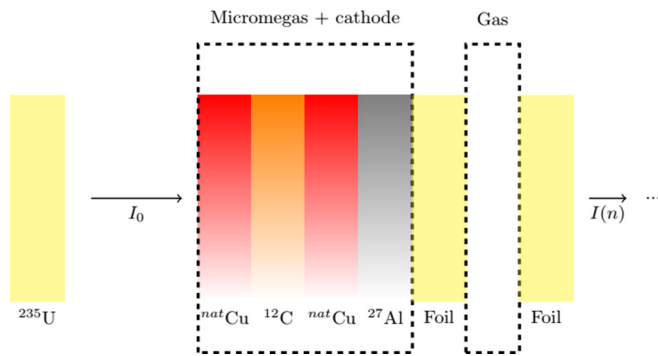
FIG. 11. The neutron self-shielding correction was based on the Beer-Lambert law and ENDF/B-VIII.0 (n,tot) cross sections for the materials seen in the figure.


FIG. 12. Correction factors for neutron beam attenuation that were applied to ^{240}Pu and ^{238}U.

5. Miscellaneous corrections

The remaining correction factors were either estimated to be negligible or did not require a complicated analysis; however a brief discussion of the their calculation will follow.

a. Self-absorption of fission fragments. Emitted fission fragments deposit an amount of their kinetic energy in the sample. A fraction of those might then produce a signal below the detection threshold, thus the fission yield is underestimated. To estimate the amount of these fission fragments, the Monte Carlo simulations described in Sec. III B 2 were used. A fraction that did not exceed 0.1% was estimated with an uncertainty that is defined by the uncertainty of the reported masses and has negligible contribution to the final cross section uncertainty. Nevertheless, at high neutron energies the fission fragment angular distribution (FFAD) might have an effect on the self-absorption and thus on the detection efficiency, as demonstrated in Refs. [47–49]. In the present case, the Monte Carlo simulations described in Sec. III B 2 were used and the fission fragments were propagated towards the gas at angles ranging from 0° to 90°. The simulations showed that the effect on the correction can be neglected.

b. Neutron beam attenuation. The neutron beam attenuation in the detector stack layers (Fig. 11), was taken into account using Beer-Lambert's attenuation law and ENDF/B-VIII.0 (n,tot) cross sections (σ_{tot}). According to the configuration shown in Fig. 11, the beam with an I_0 intensity, that exits ^{235}U, suffered successive losses when crossing a layer with n atoms/cm^2, described by the ratio seen in Eq. (4), where i denotes each layer from the exit of ^{235}U up to the corresponding fission foil:

$$\frac{f_{\text{shield}}}{f_{\text{shield}}^{(\text{ref})}} = \exp\left\{\sum_i n_i \sigma_{\text{tot},i}\right\}. \tag{4}$$

The neutron transport in the gas was neglected due to its negligible mass, therefore it is not visible in Fig. 11, and Kapton was assumed to be pure ^{12}C, which accounts for 70% of Kapton [50].

The estimated correction factors can be seen in Fig. 12. It has to be noted that the correction in ^{238}U was not applied below 1 MeV due to the absence of statistics. In addition, the uncertainty of this correction depends mainly on the
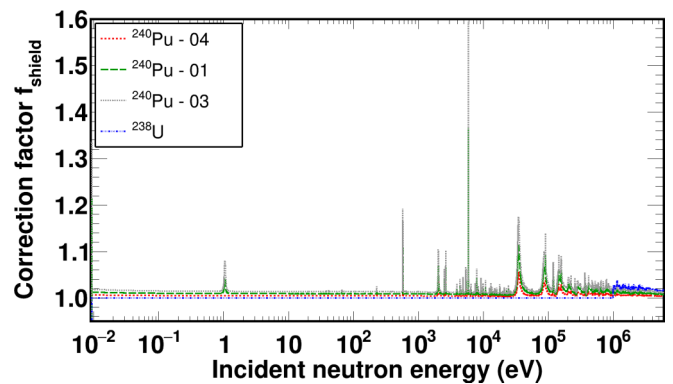
uncertainty of the evaluated cross sections and was estimated to be less than 2%, since the number of atoms was known with an accuracy better than 1%.

c. Spontaneous fission. To estimate the contribution of spontaneous fission and cluster decay, the beam-off spectra were used. It was experimentally shown that per proton bunch (Fig. 13) less than 0.4% of the recorded counts were attributed to spontaneous fission and cluster decay events. The uncertainty in this case was estimated to be 5% based on the statistical uncertainty of the recorded spontaneous fission events in the longest beam-off run, which corresponded to 50000 proton bunches. It has to be mentioned that the branching ratio of cluster decay is appreciably smaller than spontaneous fission, therefore it was neglected in the correction.

d. Photofission. To estimate the contribution of photofission events, Monte Carlo simulations were used. More specifically, the simulated photon fluence from the spallation process was used, along with the ENDF/B-VIII.0 (γ, f) cross sections, in order to calculate the expected reaction rate. Photofission events were estimated to contribute less than 0.2% in the worst case.
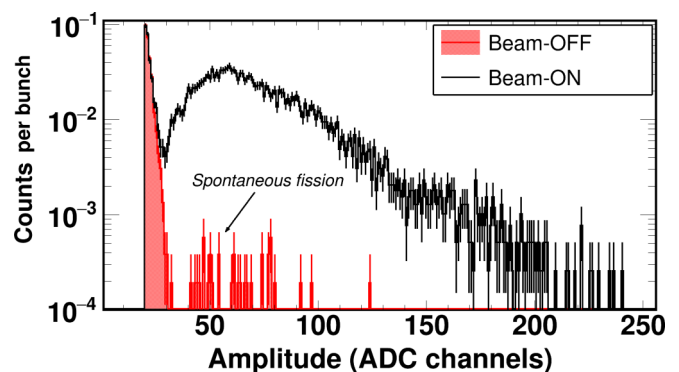
FIG. 13. Comparison between beam-on and -off spectra recorded from the most massive ^{240}Pu sample. The contribution of spontaneous fission was considered negligible. Spectra are normalized to the number of triggers for a direct comparison.
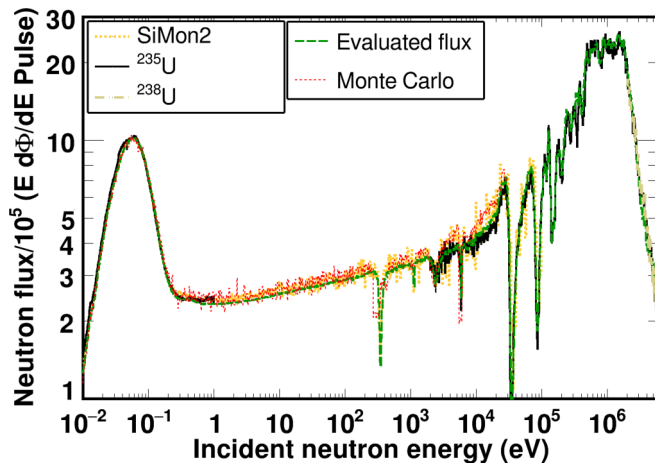
FIG. 14. The neutron flux calculated from ^{235}U, ^{238}U, and Si-Mon2 was found in satisfactory agreement with the evaluated and the simulated ones.

6. Neutron flux

In the resolved resonance region, the ^{240}Pu(n, f) cross section was calculated using the EAR2 evaluated flux [32]. The flux of the vertical neutron beam is given at the floor level of the bunker, therefore a normalization factor was applied to estimate the flux at the sample position, which was determined by the neutron flux obtained from ^{235}U.

The neutron flux was calculated using ^{235}U from 9 meV up to 6 MeV, excluding the 1 eV–2 keV resonance region. Then, the neutron flux from ^{238}U was also calculated in order to benchmark the flux calculated from ^{235}U. As shown in Fig. 14, the agreement was quite satisfactory in the MeV region, indicating that the absolute flux value was properly calculated.

Moreover, the flux was also calculated using the data obtained from SiMon2 and was normalised to ^{235}U at the thermal peak (56 meV). As shown in Fig. 14, the agreement in the overlapping energy region between SiMon2 and ^{235}U was quite satisfactory, indicating a proper reconstruction of the shape of the neutron spectrum.

The next step was to normalize the evaluated flux at the thermal peak and to examine the agreement concerning the shape of the neutron flux. As illustrated in Fig. 14, an overall agreement was observed.

Finally, to benchmark the normalization, the n_TOF simulation pool was used. Neutrons that were scored at the exit of the spallation target, were propagated towards EAR2 using an optical transport, to the position of ^{235}U. As shown in Fig. 14, the simulated flux was in agreement at the thermal peak with the ^{235}U, the evaluated, and the SiMon2 fluxes, indicating the consistency obtained by the redundant determination of the neutron flux.

As a result, the normalized evaluated flux was used to calculate the ^{240}Pu(n, f) cross section in the resolved resonance region.

In addition, the simulations were used to estimate the decrease of the neutron flux during its propagation. The flux on each fission foil was calculated and an average drop of
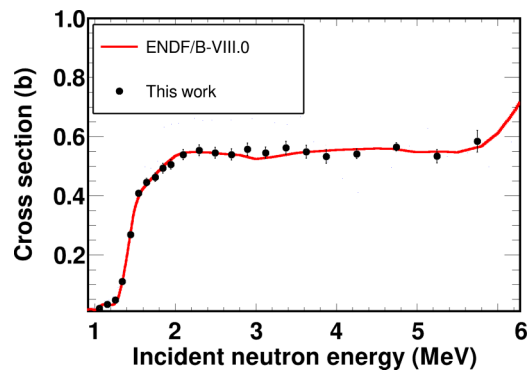
FIG. 15. The ^{238}U(n, f) cross section that was calculated with reference to the ^{235}U(n, f) one was in satisfactory agreement with the ENDF/B-VIII.0 evaluation.

0.24% per cm was estimated and taken into account in the analysis of the flux ratio. Finally, Table II summarizes the correction factors and their corresponding uncertainties.

C. Analysis benchmark

Prior to reporting the final results, a benchmarking procedure was adopted. First of all, the data from the reference foils were used to reproduce the ^{238}U(n, f) neutron standard. As shown in Fig. 15, the ^{238}U(n, f) cross section was calculated with reference to ^{235}U(n, f) and a satisfactory agreement with the ENDF/B-VIII.0 evaluation within less than 3% was achieved.

Finally, an overall agreement within uncertainties was observed between the corrected counting spectra for each sample, therefore the reported cross section was the weighted average of the individual ones.

IV. RESULTS AND DISCUSSION

The ^{240}Pu(n, f) cross section was obtained in a broad energy range that spanned from 9 meV up to 6 MeV (Fig. 16), covering almost nine orders of magnitude in neutron energy, illustrating the impressive capabilities of EAR2 for fission measurements. It has to be noted that the conversion from
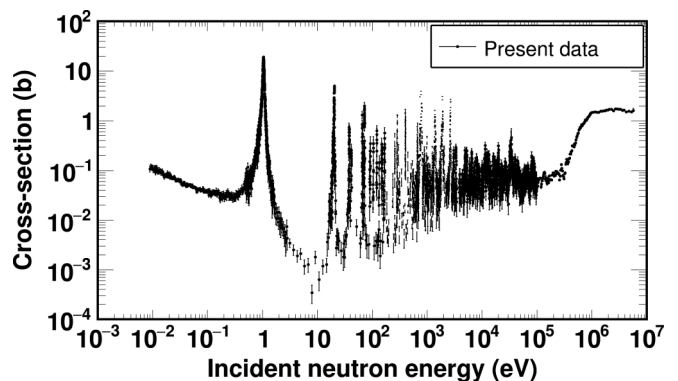
FIG. 16. The ^{240}Pu(n, f) cross section that was derived in the present work spanned across a wide range in neutron energy, from 9 meV up to 6 MeV.
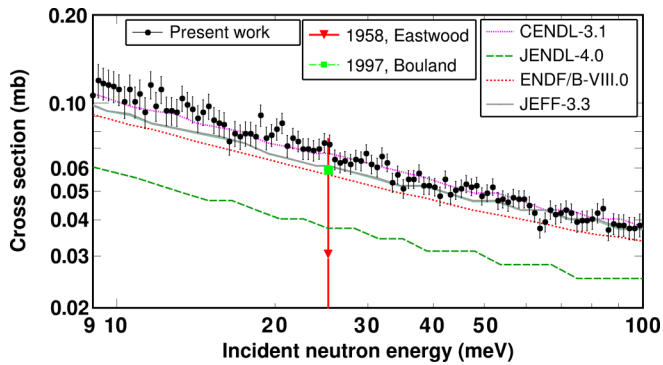
FIG. 17. The ^{240}Pu(n, f) cross section between 9 and 100 meV in comparison with the experimental data of Eastwood *et al.* [14] and the evaluation by Bouland *et al.* [19] as well as the most common evaluation libraries [52–55].

FIG. 18. The high resolution ^{240}Pu(n, f) cross section in the 1.05 eV region demonstrates the impressive capabilities of EAR2 in low energy fission measurements.

time of flight to the incident neutron energy was made by using an effective flight path L, that was estimated with the methodology described in Ref. [51]. The effective flight path was found to be 19.5 m for ^{235}U, and 0.017 m were added for each successive fission foil, which corresponds to the geometric spacing which was accurately known within 0.1%. The uncertainties shown in Fig. 16 correspond to the statistical uncertainties, after the application of the correction factors.

A. Thermal region

In the thermal region, only two measurements were reported in EXFOR, which were discrepant and with a high uncertainty as described in Sec. I B. The derived cross section between 9 and 100 meV is shown in Fig. 17 and corresponds to the only available time-of-flight data set in literature. The present data set is in a better agreement with the data point by Eastwood compared to the corresponding one by Pratt. In addition, a fair agreement within uncertainties was observed between CENDL-3.1 [52] and JEFF-3.3 [53], while ENDF/B-VIII.0 [54] was systematically lower by about 15%. Finally, JENDL-4.0 [53] underestimated the cross section by about a factor of 2. The present data set is expected to provide additional material for future evaluations, thus reducing the discrepancies among the libraries.

B. Resonance at 1.05 eV

Although a comparison in the resolved resonance region is only possible through resonance parameters, a brief discussion will follow regarding the first resonance in the ^{240}Pu(n, f) cross section at ≈ 1 eV. The only available data set was reported in 1956 by Leonard *et al.* [17], with poor resolution. The efficient α-background suppression and high instantaneous flux allowed to derive a high resolution cross section, as shown in Fig. 18, demonstrating the impressive capabilities of EAR2 as a spectrometer in low energy fission studies. Concerning the cross section in the resolved resonance region, a discussion will follow in Sec. V.
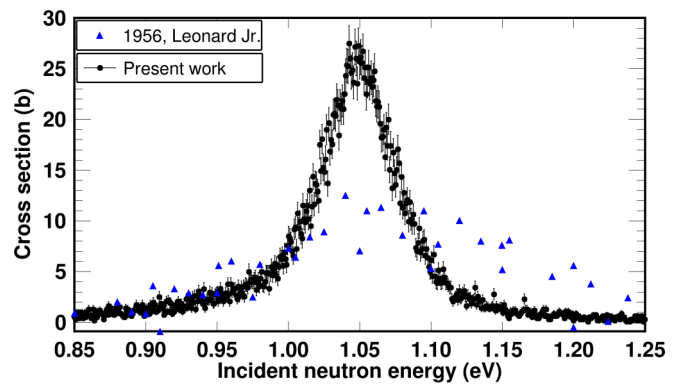
C. Unresolved resonance region

In the unresolved resonance region, between a few keV and a few tens of keV, clusters of overlapping resonances were resolved that correspond to coupling between class-I and class-II states. A typical example is shown between 10 and 30 keV (Fig. 19). The present data are in agreement with high resolution data that exist in the literature [18,20]; however, evaluated cross sections do not present any structures. The only exception is ENDF/B-VIII.0, which was clearly based on the lower resolution data reported by Tovesson *et al.* [22].

D. Fission threshold

At sub-barrier neutron energies, structures that could be attributed to vibrational bumps were observed (e.g., around 100, 140, 280, 350, 650, 785 keV), as shown in Fig. 20. An overall agreement with the latest reported data by Salvador-Castineira *et al.* [21] was observed. In addition, an overall agreement within uncertainties was observed with the data by Laptev *et al.* [23], Meadows [56], and Nesterov *et al.* [57], while the data set reported by Tovesson *et al.* [22] was
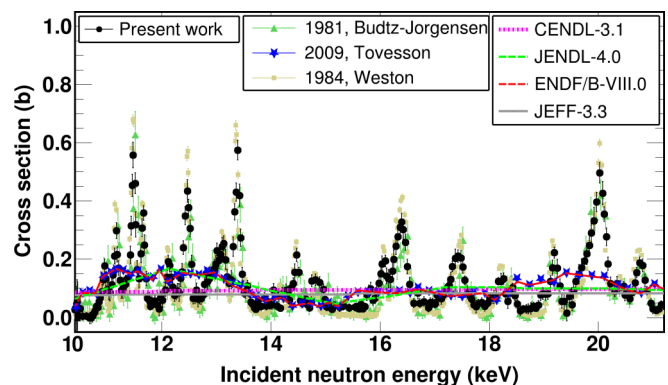
FIG. 19. The cross section in the 10–21 keV energy region. It is evident that, despite the availability of high resolution data, the observed structures are only considered in the ENDF/B-VIII.0 evaluation [54].
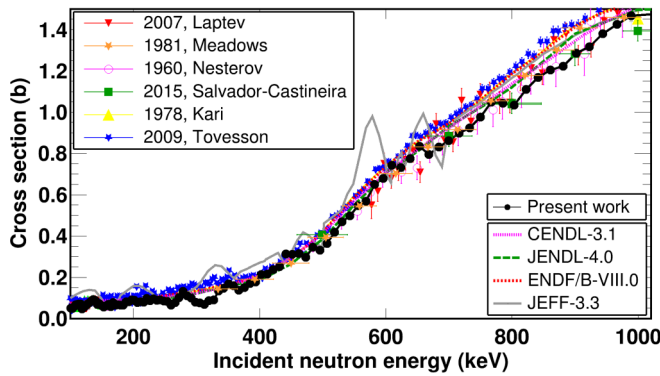
FIG. 20. The cross section in the 100 keV–1 MeV region. An overall agreement with reported data sets was observed apart from the one reported by Tovesson *et al.* [22].

FIG. 22. The correlations of the ^{240}Pu(n, f) cross section, which were calculated by means of covariance propagation.

systematically higher by 10–15%, depending on the energy range.

The evaluations are in overall agreement with each other and provide cross sections that lie between the experimental data. The present data set is expected to provide useful additional material to correct future evaluations. In addition to the previous comparison, the evaluated cross sections did not predict the subthreshold structures that were observed in the present data. The only exception is JEFF-3.3 which shows some structures; however, they seem unrealistically pronounced.

E. First chance fission

In the energy region between 1 and 6 MeV, the derived cross section is in agreement within uncertainties with the data reported by Salvador-Castineira *et al.* [21], Laptev *et al.* [23], and Meadows [56], as shown in Fig. 21. Up to 2.7 MeV, the systematic discrepancy concerning the data by Tovesson *et al.* [22] was still present, while above 4 MeV the uncertainty in the present data set did not allow us to draw any conclusions. The same remarks are also valid regarding the data set by Kari *et al.* [58–60], since it is in agreement with the one by Tovesson *et al.* [22].

FIG. 21. Comparison of the cross section in the 1–6 MeV region with the respective statistical uncertainties.

An interesting dip around 2.5 MeV was observed not only in the present work, but also in the data of Laptev *et al.* [23], Cance *et al.* [61], and Kazarinova *et al.* [62]. Its origin is not yet understood, therefore further investigation would be justified.

Finally, concerning the evaluations, an overall agreement with JENDL-4.0 was observed across the first chance fission plateau. A slightly worse agreement between the present data and CENDL-3.1 was observed, due to the underestimated evaluated cross section between 2.3 and 3.6 MeV. JEFF-3.3 overestimated the fission cross section and exhibited an overall smoother behavior than the one observed in the present work and previous experimental data. Finally, ENDF/B-VIII.0 lies between the reported data, following the trend of the data by Tovesson *et al.* [22].

It has to be noted that the larger statistical uncertainties in the 4–6 MeV energy region are attributed to the fact that the cross section was calculated using only one ^{240}Pu sample, since in all others the γ-flash subtraction and counting loss correction could only be applied up to 4 MeV.

F. Covariance propagation

The cross section calculation was accompanied by the estimation of the uncertainties and correlations. In this respect only non-negligible components were taken into account, such as the fission counts, f_{amp}, f_{imp}, the mass m, the neutron flux in the 800 meV–2 keV region, and f_{DT} above 1 MeV. The fission counts and the neutron flux were considered to have a fully uncorrelated contribution to the covariance matrix while f_{amp} and m have correlated components. Regarding f_{imp}, its covariance matrix was calculated separately assuming that the biggest contribution was the atomic abundances, neglecting therefore the uncertainty of the known ^{239}Pu(n, f) cross section.

The covariance matrix was used to estimate the total uncertainty, which is reported in Appendix B, and the correlations in the cross section. The estimated correlations are illustrated in Fig. 22.

V. RESONANCE ANALYSIS

Between 1 eV and 10 keV a total of 25 fission resonances were resolved with sufficient statistical accuracy. Due to the nature of the double humped fission barrier, fission resonances are grouped, resulting in a significant fluctuation of fission widths which justifies the analysis of only strong resonances.

A. Details of the resonance analysis

The resolved resonances were analysed by means of the SAMMY code [63] implementing the R-matrix formalism. The present analysis was performed under the following assumptions: (a) the Reich-Moore approximation was selected, (b) Doppler broadening was taken into account using the free gas model ($T = 300$ K), (c) multiple scattering effects were neglected due to the small thickness of the samples compared to the mean neutron path, and (d) broadening due to the time resolution of the spectrometer was used taking into account both the proton burst width (7 ns RMS) and the neutron transport within the target-moderator assembly, which was obtained from Monte Carlo simulations [64].

As far as the calculation is concerned, resonances were considered to be s waves ($l = 0$). In addition, since fission widths (Γ_f) in a nonfissile nucleus are appreciably smaller than the neutron (Γ_n) and capture (Γ_γ) widths, the present data could not provide Γ_n and Γ_γ. Therefore, up to 5.7 keV, Γ_n and Γ_γ were fixed to the values proposed by Bouland et al. [19], which are the ones adopted by ENDF/B-VIII.0 and JEFF-3.3, while the neutron energy E_n and Γ_f were fitted.

Above 5.7 keV, in the absence of resonance parameters in literature, a constant radiation width of 31.8 meV was adopted from ENDF/B-VIII.0. Despite the existence of transmission data by Gwin [65], neutron widths were also absent in literature. In this respect, a constant reduced neutron width was used, which was calculated considering a mean level spacing $\langle D \rangle = 12.06(60)$ eV and the strength function $S_0 = 1.032(71)10^{-4}$ proposed by Bouland et al. [19], using

$$g_J \Gamma_n^0 = S_0 \langle D \rangle \sqrt{E_n}, \tag{5}$$

where g_J is the spin factor and in the present work had a value of 1 since only s waves were considered.

The neutron energy was fitted using a fudge factor of $0.01 = 1\%$ and an overall agreement with the evaluation of Bouland et al. [19] was observed. In contrast, fission widths were left practically free to vary using a fudge factor of 10. The uncertainty in the varying parameters was provided by SAMMY as the uncertainty of the propagated uncertainty parameters (PUP in SAMMY notation).

It has to be noted that the broadening induced by the neutron moderation did not allow the determination of Γ_f unless it was much greater than Γ_n and Γ_γ, therefore the fission kernels F_K will be reported, which were calculated using

$$F_K = g_J \frac{\Gamma_f \Gamma_n}{\Gamma_f + \Gamma_n + \Gamma_\gamma}. \tag{6}$$

TABLE III. List of the fission kernels with a statistical uncertainty of less than 30%. Negative differences correspond to a smaller fission kernel compared to the corresponding one by Bouland et al. [19].

E_n (eV)	Fission kernel (meV)			
	Present work	Relative uncertainty (%)	Bouland et al. [19]	Difference (%)
1.06	0.00059(8)	14	0.00063	−6
20.4	0.027(6)	20	0.019	35
38.4	0.0078(7)	9	0.0043	59
66.6	0.021(1)	5	0.016	25
72.8	0.044(2)	5	0.041	8
152.0	0.099(2)	2	0.094	6
260.5	0.048(2)	4	0.038	26
287.0	0.30(5)	17	0.30	−2
405.0	0.33(6)	18	0.36	−8
743.1	0.017(3)	18	0.040	−81
750.3	8.2(2)	2	6.9	17
778.1	0.020(1)	5	0.019	5
783.1	3.3(6)	18	3.8	−14
790.5	5.5(2)	4	5.7	−4
1402	9.4(1)	1	9.6	−2
1842	8.2(3)	4	7.7	6
1902	3.2(2)	6	2.8	12
1917	20(2)	10	21	−4
1948	7.5(2)	3	6.0	22
1955	17.8(4)	2	20	−13
2033	10.3(25)	24	6.6	43
2698[a]	82(8)	10	77	6
6551	12.5(3)	2		
7508	64.5(5)	1		
8098	111(9)	8		

[a]Resonance energy was found to be higher by 4 eV.

B. Results and discussion

The discussion that follows concerns resolved resonances with sufficient statistical accuracy and fission kernels with an uncertainty less than 30%. Other, perhaps doubtful, resonances were accepted in the analysis and their parameters, which were calculated with an uncertainty higher than 30%, can be retrieved in Appendix A, where the parametrization of the present cross section is provided.

In the following figures, a comparison is presented (top panels) between the experimental data, the fits obtained by SAMMY, and the evaluated cross section by Bouland et al. [19] which was broadened using the response function of EAR2. In the bottom panels, the residuals between the SAMMY fits and the experimental data are given. In Table III the fission kernels are reported, while a full parametrization of the cross section is given in Appendix A.

1. Resonance at 1.05 eV

The extracted Γ_f at the first resonance at 1.05 eV was 0.0077(4) meV, which is roughly 6% smaller than the
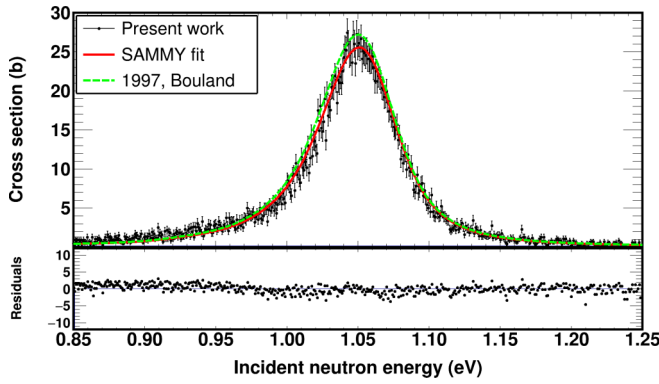
FIG. 23. Resonance at 1.05 eV where a fission width with a 5% uncertainty was derived.

0.0081(15) meV reported by Bouland *et al.* [19]; see also Fig. 23.

2. Energy region between 19 and 400 eV

In this energy region, five typical examples of fission resonances are presented in Fig. 24. The analysis of the second isolated resonance at 20.4 eV [Fig. 24(a)], provided a fission width $\Gamma_f = 0.29$ meV, that is higher by 30% compared to the 0.20 meV proposed by Bouland *et al.* The uncertainty in Γ_f, mainly attributed to statistics, cannot justify this discrepancy. In addition, in this energy region, the corrections were quite small, therefore the present fission width is considered to be accurate. The same was observed for an isolated resonance at 38.4 eV, where the extracted fission width is 0.017 meV and the evaluated one 0.0095 meV. The 45% discrepancy clearly exceeds the 20% statistical uncertainty.

A resonance at 152 eV was also resolved, with a fission width of 0.38 meV, 5% higher than the corresponding value of Bouland *et al.* who reported Γ_f equal to 0.36 meV. The statistical uncertainty in the Γ_f calculation of the present work was of the order of 6%, therefore both values were in agreement within uncertainties, as illustrated in Fig. 24(b).

Two isolated resonances were also resolved at 260.5 and 286.9 eV, as shown in Fig. 24(c). The resonance analysis yielded fission widths of 0.12 and 0.37 meV respectively while the corresponding ones from Bouland *et al.* were 0.09 and 0.38 meV, respectively. In the former resonance, a 25% discrepancy was observed which could be attributed to the 30% statistical accuracy while in the latter the present data confirm Bouland's *et al.* evaluation.

Finally, an 8% discrepancy was observed for the 405 eV resonance for which Bouland *et al.* proposed $\Gamma_f = 0.47$ meV compared to the 0.43 meV extracted from the present work. In this case the statistical uncertainty was of the order of 25%, therefore both fission kernels were compatible within uncertainties, as illustrated in Fig. 24(d).

All in all, fair agreement within uncertainties was observed compared to the evaluation by Bouland *et al.* The limitation of statistical accuracy cannot provide a clear confirmation of the resonance parameters reported by Bouland *et al.*; however, the
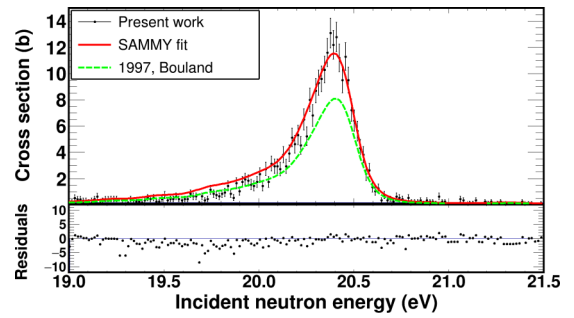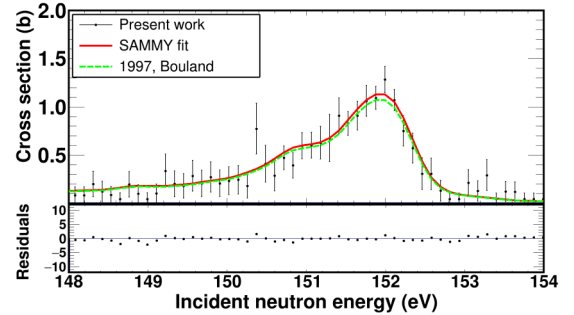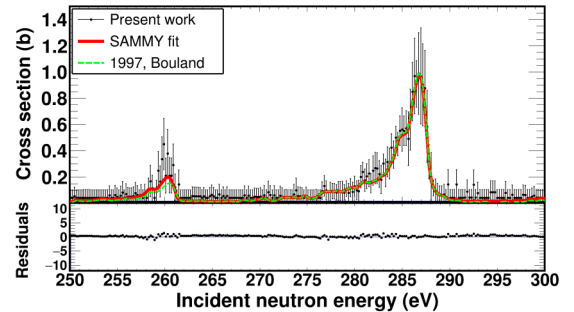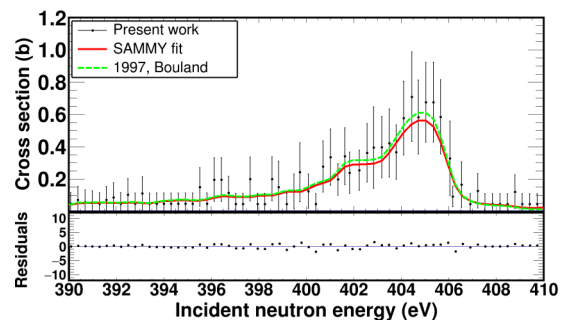
FIG. 24. A few resonances that were resolved in the 19–400 eV region. (a) Resonance at 20.4 eV. (b) Resonance at 152 eV. (c) Isolated class-I resonances at 260.2 and 286.9 eV. (d) Resonance at 405 eV. An overall agreement within uncertainties was observed with the evaluation by Bouland *et al.* [19], except for the resonance at 20.4 eV. See text for further details.

discrepancy observed at the 20.4 eV resonance indicates an underestimation of the fission cross section, therefore further investigation is recommended.

(a)

(b)
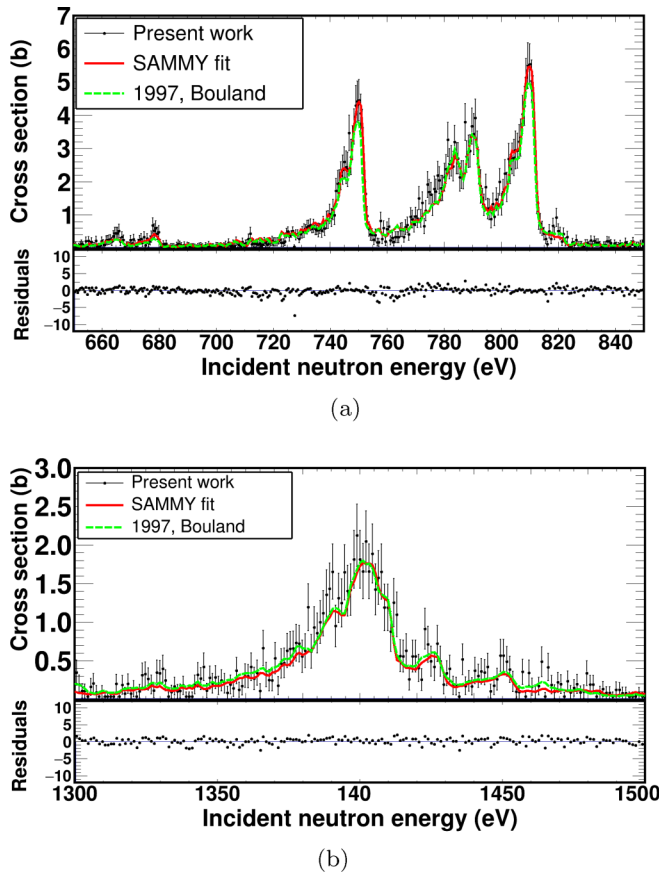
FIG. 25. Cross sections in regions where resonances with high fission widths were observed. (a) The cross section close to the 782 eV resonance. (b) The cross section close to the 1402 eV resonance.

3. Resonances with large fission widths

In fission resonances where the fission width is notably higher than Γ_n and Γ_γ, Eq. (6) is reduced to

$$F_K \approx g_J \Gamma_n, \tag{7}$$

which implies that the resonance area is sensitive to the neutron width. In addition the determination of the fission width can be achieved by transmission measurements, since in this case the total width Γ is practically equal to Γ_f. Among such resonances, two were resolved at 782 and 1402 eV. Apart from Bouland *et al.* [19], Guerrero *et al.* [66] provided resonance parameters, analyzing capture data from n_TOF [67] and transmission data from Kolar and Böckhoff [68].

In these resonances, the radiation widths proposed by Bouland *et al.* and Guerrero were adopted along with the common fission widths they used. The neutron widths were left free to vary.

a. Resonance at 783 eV. Concerning the 783 eV resonance, which can be seen in Fig. 25(a), Bouland *et al.* [19] proposed a neutron width which was equal to 3.83 meV and a 31.2 meV radiation width. Guerrero *et al.* [66] proposed a radiation width of 36.6 meV, and the analysis of the transmission data of Kolar and Böckhoff yielded a width of 6.26 meV.
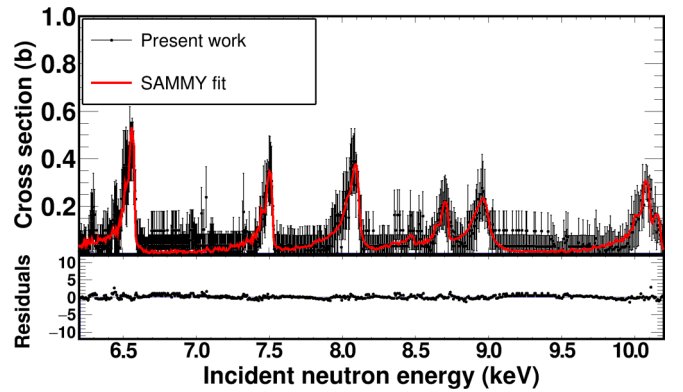
FIG. 26. Prominent resonance structures that were observed between 6.2 and 10.2 keV. A parametrization of the cross section is provided in Appendix A using Reich-Moore resonance parameters.

Both reported a fission width $\Gamma_f = 1858$ meV, which was adopted in this work. The present analysis yielded a 3.3 meV fission kernel using Γ_γ and Γ_f from Bouland *et al.*, which was 14% smaller than the evaluated value. The Γ_n that was derived using Guerrero's Γ_γ was 3.88 meV, which practically confirms the neutron width by Bouland *et al.* The Γ_n extracted from the analysis of the transmission data was 53% larger than the one derived from the present analysis.

The neighboring resonances were analysed using the procedure described in the beginning of Sec. V A, therefore the Γ_f were fitted. The results are reported in Table IV.

b. Resonance at 1402 eV. The neutron widths proposed by Bouland *et al.* [19] and Guerrero *et al.* [66] were 9.83 and 10.02 meV, respectively, while Γ_γ was practically the same (31.8 and 31.0 meV, respectively). Both used a fission width of 2085.5 meV, which was adopted in the present work. The fission kernel that was estimated from the present work was 9.4 meV and is in agreement with the values derived by Guerrero *et al.* [66] and Bouland *et al.* [19], as illustrated in Fig. 25(b).

4. Resonances beyond evaluations

Bouland *et al.* extracted resonance parameters up to 5.7 keV; however, in the present data prominent resonance structures were resolved at higher energies, even up to 20 keV. An example is shown in Fig. 26 in the 6.2–10.2 keV energy region. The corresponding parametrization of the cross section is given in Appendix A by means of Reich-Moore resonance parameters. It has to be noted that, in this overlapping region, resonances are Ericson type fluctuations and the fission kernels reflect some fission mixtures of the coherent mixing of a set of overlapping compound states.

C. Remarks on the resonance analysis

The resonance analysis that was presented demonstrated the capability of measurements in EAR2 in resolving fission resonances. Although the experiment was not originally designed to achieve the required statistical accuracy for resonance analyses, the parameters from the present data were

in overall agreement with the evaluation by Bouland *et al.* [19], including fission and neutron widths. On top of that, new and/or more accurate resonance parameters could be proposed. The resulting fission kernels which were extracted with a statistical accuracy better than 30% are listed in Table III, in comparison to the ones proposed by Bouland *et al.*

VI. CONCLUSION

The second experimental area (EAR2, 19 m flight path) was commissioned in 2014 [25] in order to expand the measuring capabilities of CERN's n_TOF facility in studying reactions where high activity and/or low mass samples are involved. In this respect, the first experiment that was performed was the study of the ^{240}Pu(n, f) cross section, which could not be completed in a previous measurement in the existing experimental area (EAR1, 185 m flight path) due to the detector deterioration induced by the long exposure to the activity of the fission foils [24].

The present measurement was successfully completed and yielded a cross section in a broad energy range from 9 meV up to 6 MeV incident neutron energy, covering almost nine orders of magnitude. This experimental campaign demonstrated the capabilities of EAR2 for measurements especially at neutron energies below the fission threshold, where the limited amount of fission material makes the study of resonances and thermal cross sections challenging. The high instantaneous neutron flux, which was delivered in a short time interval, compensated for this experimental limitation, thus appreciably reducing the intrinsic background from the α activity and providing a sufficient fission rate to observe resonance structures.

These structures were analysed by means of SAMMY fits [63], incorporating the R-matrix formalism. A total of 25 resonance kernels are reported although the experiment was not initially designed for sub-barrier fission. The majority of fission kernels is in agreement with evaluations [19], while three new values could be determined and recommended.

In the near-threshold region, resonance structures were also observed which correspond to overlapping class-II states, but they could not be analyzed using the available statistical model codes.

Above the fission threshold, the high instantaneous fission rate resulted in appreciably large counting losses, which were estimated by means of a dedicated methodology that was applied to the fission counts [45]. The derived cross section is in agreement with the latest data set by Salvador-Castineira *et al.* [21] and the time-of-flight data by Laptev *et al.* [23] but is systematically smaller than the latest time-of-flight measurement by Tovesson *et al.* [22] and the ENDF/B-VIII.0 and JEFF-3.3 evaluations. An overall agreement was observed with the CENDL-3.1 and JENDL-4.0 evaluation libraries.

The present measurement is expected to provide additional material for the evaluated libraries while emphasizing the need for an additional study in the resolved resonance region. The further upgrade of the n_TOF spallation target is expected to offer an increased neutron flux and a significantly better resolution.

Finally, due to the substantially higher instantaneous flux especially near thermal energies, EAR2 is expected to fa-

cilitate the measurement of new fission cross section data concerning actinides, which are important both in nuclear energy applications and fundamental research.

APPENDIX A: REICH-MOORE RESONANCE PARAMETERS

The resonance parameters that reproduce the reported cross sections are given in Table IV. Each file line corresponds to the parameters of one resonance. From left to right the columns contain the energy, radiation, neutron, and fission widths of each resonance. The first five fictitious resonances were adopted from Bouland *et al.* [19] and were used to simulate the contributions of external resonances. The sign in the fission widths is used to indicate the definite amplitude of fission.

TABLE IV. Resonance parameters that were used to parametrize the ^{240}Pu(n, f) cross section. The resonances were considered s waves, therefore the resonance spins are $J = 1/2$.

Energy (eV)	Γ_γ (meV)	Γ_n (meV)	Γ_f (meV)
-4.070×10^3	3.18×10^1	3.55×10^4	3.37×10^{-3}
-1.300×10^3	3.18×10^1	3.52×10^3	-4.31×10^{-2}
-3.050×10^2	3.18×10^1	2.14×10^2	4.00×10^{-2}
-7.010×10^1	3.18×10^1	3.09×10^2	-4.00×10^{-2}
-3.000×10^0	3.91×10^1	1.31×10^0	1.00×10^{-3}
1.058×10^0	2.91×10^1	2.45×10^0	7.65×10^{-3}
2.043×10^1	2.70×10^1	2.75×10^0	-2.90×10^{-1}
3.835×10^1	2.40×10^1	1.96×10^1	1.74×10^{-2}
4.175×10^1	2.55×10^1	1.74×10^1	7.11×10^{-3}
6.664×10^1	3.30×10^1	5.55×10^1	3.27×10^{-2}
7.277×10^1	2.64×10^1	2.17×10^1	9.78×10^{-2}
9.078×10^1	3.08×10^1	1.33×10^1	-1.01×10^{-2}
9.249×10^1	2.83×10^1	3.00×10^0	-6.32×10^{-2}
1.050×10^2	2.85×10^1	4.62×10^1	-5.10×10^{-3}
1.217×10^2	3.36×10^1	1.49×10^1	8.70×10^{-2}
1.257×10^2	3.18×10^1	1.20×10^{-1}	-2.00×10^{-2}
1.308×10^2	3.09×10^1	1.79×10^{-1}	2.41×10^{-1}
1.351×10^2	3.29×10^1	1.83×10^1	4.83×10^{-2}
1.520×10^2	3.75×10^1	1.35×10^1	3.77×10^{-1}
1.627×10^2	2.91×10^1	8.48×10^0	1.58×10^0
1.698×10^2	3.10×10^1	1.32×10^1	-1.37×10^{-1}
1.858×10^2	3.10×10^1	1.58×10^1	8.95×10^{-3}
1.920×10^2	3.06×10^1	2.85×10^{-1}	-1.28×10^{-1}
1.956×10^2	3.18×10^1	1.60×10^{-1}	1.20×10^{-1}
1.974×10^2	3.18×10^1	1.60×10^{-1}	-1.20×10^{-1}
1.997×10^2	2.86×10^1	9.70×10^{-1}	1.37×10^{-1}
2.389×10^2	2.87×10^1	1.19×10^1	1.35×10^{-1}
2.605×10^2	3.28×10^1	2.23×10^1	-1.19×10^{-1}

TABLE IV. *(Continued.)*

TABLE IV. *(Continued.)*

Energy (eV)	Γ_γ (meV)	Γ_n (meV)	Γ_f (meV)	Energy (eV)	Γ_γ (meV)	Γ_n (meV)	Γ_f (meV)
2.869×10^2	3.20×10^1	1.35×10^2	-3.69×10^{-1}	9.713×10^2	2.99×10^1	7.98×10^1	6.00×10^{-2}
3.049×10^2	3.39×10^1	7.37×10^0	2.12×10^{-1}	9.792×10^2	3.18×10^1	7.20×10^0	-4.37×10^{-1}
3.136×10^2	3.18×10^1	1.20×10^{-1}	-2.50×10^{-1}	9.830×10^2	3.18×10^1	1.00×10^0	4.80×10^1
3.181×10^2	3.22×10^1	5.23×10^0	3.21×10^{-1}	9.919×10^2	3.18×10^1	3.00×10^{-1}	2.67×10^4
3.207×10^2	3.49×10^1	1.89×10^1	-3.26×10^{-2}	1.002×10^3	2.98×10^1	9.73×10^1	-1.56×10^0
3.327×10^2	3.18×10^1	1.30×10^{-1}	2.49×10^{-2}	1.012×10^3	3.18×10^1	2.00×10^0	8.11×10^0
3.383×10^2	3.14×10^1	5.94×10^0	-4.57×10^{-3}	1.024×10^3	3.18×10^1	5.23×10^0	8.05×10^{-1}
3.459×10^2	3.39×10^1	1.59×10^1	3.52×10^{-1}	1.029×10^3	3.18×10^1	2.00×10^0	4.53×10^0
3.635×10^2	3.88×10^1	3.16×10^1	1.37×10^{-1}	1.037×10^3	3.18×10^1	2.00×10^0	-2.17×10^0
3.719×10^2	3.04×10^1	1.33×10^1	-1.35×10^{-1}	1.042×10^3	2.97×10^1	1.21×10^1	-1.70×10^{-1}
3.930×10^2	3.18×10^1	1.50×10^{-1}	-1.70×10^{-2}	1.046×10^3	3.18×10^1	3.94×10^0	2.47×10^0
4.050×10^2	3.24×10^1	1.03×10^2	-4.31×10^{-1}	1.051×10^3	3.18×10^1	2.00×10^0	7.49×10^0
4.189×10^2	3.09×10^1	5.77×10^0	2.87×10^{-1}	1.072×10^3	2.91×10^1	1.09×10^2	-2.72×10^{-1}
4.457×10^2	3.14×10^1	1.84×10^0	-5.84×10^{-1}	1.077×10^3	3.18×10^1	1.70×10^0	-1.85×10^0
4.498×10^2	3.22×10^1	1.61×10^1	1.47×10^{-1}	1.086×10^3	3.18×10^1	2.00×10^0	2.21×10^0
4.666×10^2	3.29×10^1	2.65×10^0	1.03×10^0	1.100×10^3	3.41×10^1	8.00×10^1	-3.04×10^{-1}
4.733×10^2	3.07×10^1	4.11×10^0	1.00×10^0	1.116×10^3	3.18×10^1	2.57×10^0	-5.47×10^{-1}
4.938×10^2	3.15×10^1	5.35×10^0	-5.30×10^{-1}	1.129×10^3	3.09×10^1	4.98×10^1	6.72×10^{-1}
4.989×10^2	3.63×10^1	1.85×10^1	2.08×10^{-1}	1.134×10^3	3.18×10^1	6.97×10^0	3.62×10^{-1}
5.100×10^2	3.18×10^1	4.14×10^{-1}	6.40×10^{-2}	1.143×10^3	3.10×10^1	4.22×10^1	-4.22×10^{-1}
5.125×10^2	3.18×10^1	5.17×10^{-1}	-4.47×10^{-2}	1.160×10^3	3.29×10^1	2.38×10^1	-6.87×10^{-1}
5.145×10^2	3.36×10^1	2.09×10^1	-2.06×10^{-1}	1.176×10^3	3.18×10^1	1.50×10^0	4.12×10^0
5.263×10^2	3.18×10^1	9.61×10^{-1}	1.00×10^0	1.186×10^3	3.21×10^1	1.59×10^2	1.11×10^{-1}
5.308×10^2	3.18×10^1	6.77×10^{-1}	2.92×10^0	1.191×10^3	3.18×10^1	1.14×10^2	-1.46×10^{-1}
5.463×10^2	3.99×10^1	3.11×10^1	-9.97×10^{-2}	1.201×10^3	3.18×10^1	2.00×10^0	1.40×10^0
5.534×10^2	3.48×10^1	1.79×10^1	3.95×10^{-1}	1.209×10^3	3.17×10^1	6.25×10^1	-3.50×10^{-1}
5.665×10^2	3.38×10^1	3.14×10^1	-2.79×10^{-1}	1.228×10^3	3.18×10^1	1.04×10^1	9.40×10^{-1}
5.844×10^2	3.18×10^1	1.15×10^0	3.61×10^0	1.237×10^3	3.18×10^1	1.12×10^1	7.82×10^{-1}
5.966×10^2	3.72×10^1	5.42×10^1	1.22×10^{-1}	1.256×10^3	3.12×10^1	7.99×10^1	-4.52×10^0
6.080×10^2	2.91×10^1	2.22×10^1	-9.02×10^{-2}	1.281×10^3	3.18×10^1	4.20×10^0	-1.01×10^0
6.322×10^2	3.24×10^1	1.35×10^1	-4.07×10^{-1}	1.301×10^3	3.06×10^1	2.49×10^2	-2.67×10^{-1}
6.376×10^2	3.06×10^1	1.19×10^1	-1.16×10^{-1}	1.328×10^3	3.27×10^1	3.68×10^2	5.07×10^{-1}
6.498×10^2	3.18×10^1	1.20×10^0	2.20×10^0	1.345×10^3	3.18×10^1	2.49×10^1	1.09×10^{-1}
6.657×10^2	2.74×10^1	2.03×10^2	-3.59×10^{-1}	1.351×10^3	3.18×10^1	7.74×10^0	-2.72×10^{-2}
6.789×10^2	3.20×10^1	2.54×10^1	-1.31×10^0	1.363×10^3	3.18×10^1	7.31×10^0	2.78×10^{-1}
7.121×10^2	3.18×10^1	1.33×10^0	3.26×10^{-1}	1.377×10^3	3.12×10^1	6.61×10^1	-1.13×10^{-1}
7.433×10^2	3.18×10^1	1.01×10^0	5.60×10^{-1}	1.389×10^3	3.18×10^1	1.47×10^1	6.30×10^0
7.503×10^2	3.25×10^1	6.95×10^1	-1.36×10^1	1.402×10^3	3.10×10^1	9.58×10^0	-2.09×10^3
7.589×10^2	3.20×10^1	5.82×10^0	1.68×10^{-1}	1.408×10^3	3.18×10^1	9.91×10^0	-8.52×10^1
7.783×10^2	3.18×10^1	1.12×10^0	5.85×10^{-1}	1.426×10^3	2.99×10^1	3.91×10^1	5.49×10^0
7.829×10^2	3.12×10^1	3.33×10^0	-1.86×10^3	1.429×10^3	3.18×10^1	1.57×10^1	-1.02×10^0
7.905×10^2	2.32×10^1	2.52×10^1	-1.34×10^1	1.442×10^3	3.18×10^1	2.00×10^0	6.74×10^0
8.103×10^2	3.73×10^1	2.20×10^2	1.55×10^1	1.450×10^3	3.18×10^1	2.69×10^1	-1.49×10^0
8.200×10^2	2.98×10^1	1.11×10^2	6.46×10^{-1}	1.451×10^3	3.15×10^1	2.74×10^1	-2.74×10^0
8.333×10^2	3.18×10^1	1.02×10^0	-3.50×10^0	1.463×10^3	3.18×10^1	2.18×10^1	3.72×10^{-1}
8.456×10^2	3.36×10^1	9.48×10^0	1.24×10^{-1}	1.466×10^3	3.18×10^1	2.00×10^0	-2.73×10^0
8.550×10^2	3.47×10^1	4.71×10^1	-3.33×10^{-1}	1.475×10^3	3.18×10^1	2.00×10^0	-4.67×10^0
8.680×10^2	3.18×10^1	1.02×10^0	1.42×10^0	1.481×10^3	3.18×10^1	9.76×10^0	2.01×10^0
8.764×10^2	3.29×10^1	1.45×10^1	7.68×10^{-1}	1.498×10^3	3.18×10^1	2.00×10^0	4.27×10^0
8.917×10^2	3.23×10^1	9.47×10^1	-9.35×10^{-1}	1.503×10^3	3.18×10^1	4.00×10^0	-1.11×10^{-1}
9.000×10^2	3.18×10^1	1.00×10^0	-1.20×10^1	1.529×10^3	3.18×10^1	5.00×10^0	3.25×10^0
9.040×10^2	3.48×10^1	2.21×10^1	-7.32×10^{-1}	1.540×10^3	3.23×10^1	1.02×10^2	-1.60×10^{-1}
9.089×10^2	3.22×10^1	7.79×10^1	3.24×10^{-2}	1.549×10^3	3.17×10^1	1.62×10^2	4.11×10^{-1}
9.152×10^2	3.48×10^1	3.59×10^1	-3.40×10^{-1}	1.555×10^3	3.18×10^1	2.50×10^0	-3.64×10^0
9.435×10^2	3.27×10^1	1.23×10^2	-2.98×10^{-1}	1.564×10^3	3.04×10^1	1.18×10^2	-1.20×10^{-1}
9.584×10^2	3.10×10^1	7.39×10^1	7.04×10^{-2}	1.575×10^3	3.16×10^1	1.26×10^2	-5.10×10^0
9.700×10^2	3.18×10^1	1.00×10^0	5.00×10^0	1.582×10^3	3.18×10^1	3.00×10^0	1.10×10^{-1}

TABLE IV. *(Continued.)*

Energy (eV)	Γ_γ (meV)	Γ_n (meV)	Γ_f (meV)
1.600×10^3	3.18×10^1	2.00×10^0	-1.01×10^{-1}
1.610×10^3	3.18×10^1	3.60×10^1	7.25×10^{-1}
1.621×10^3	3.18×10^1	2.80×10^1	-3.70×10^{-1}
1.629×10^3	3.18×10^1	5.00×10^0	8.37×10^{-1}
1.643×10^3	3.17×10^1	1.11×10^2	9.52×10^{-1}
1.663×10^3	3.22×10^1	6.91×10^1	-7.91×10^{-1}
1.667×10^3	3.18×10^1	6.00×10^0	1.12×10^{-1}
1.688×10^3	3.18×10^1	3.53×10^1	-1.89×10^0
1.707×10^3	3.18×10^1	4.50×10^0	1.43×10^0
1.724×10^3	3.14×10^1	8.44×10^1	1.79×10^0
1.749×10^3	3.18×10^1	3.00×10^0	-9.90×10^{-2}
1.742×10^3	3.18×10^1	2.48×10^1	7.81×10^{-1}
1.764×10^3	3.18×10^1	5.55×10^1	-2.68×10^{-1}
1.772×10^3	3.18×10^1	9.73×10^0	9.92×10^{-2}
1.779×10^3	3.07×10^1	4.87×10^2	-4.53×10^{-2}
1.789×10^3	3.18×10^1	5.00×10^0	8.02×10^{-1}
1.811×10^3	3.18×10^1	5.00×10^0	7.41×10^{-1}
1.842×10^3	3.31×10^1	1.28×10^2	-1.10×10^1
1.853×10^3	3.18×10^1	3.39×10^1	-1.26×10^0
1.862×10^3	3.18×10^1	4.00×10^0	-1.01×10^{-1}
1.873×10^3	3.07×10^1	8.07×10^1	4.14×10^0
1.886×10^3	3.18×10^1	5.00×10^0	-2.28×10^0
1.902×10^3	3.18×10^1	2.18×10^2	3.71×10^0
1.917×10^3	3.06×10^1	3.52×10^1	8.70×10^1
1.939×10^3	3.10×10^1	1.31×10^0	-1.81×10^3
1.943×10^3	3.18×10^1	7.93×10^0	1.74×10^1
1.948×10^3	3.18×10^1	8.58×10^1	1.12×10^1
1.955×10^3	3.08×10^1	2.76×10^2	-2.12×10^1
1.974×10^3	3.18×10^1	7.16×10^1	1.76×10^0
1.991×10^3	3.07×10^1	1.18×10^2	-4.79×10^{-2}
1.999×10^3	3.18×10^1	5.40×10^0	4.76×10^{-2}
2.017×10^3	3.15×10^1	5.50×10^1	-3.98×10^{-1}
2.023×10^3	2.87×10^1	6.02×10^1	1.83×10^0
2.033×10^3	3.23×10^1	1.11×10^2	1.46×10^1
2.038×10^3	3.18×10^1	5.00×10^0	1.16×10^{-1}
2.054×10^3	2.84×10^1	7.25×10^1	-5.76×10^0
2.061×10^3	3.10×10^1	5.00×10^0	8.57×10^{-2}
2.083×10^3	3.09×10^1	9.91×10^1	-1.53×10^{-1}
2.097×10^3	3.18×10^1	1.00×10^1	6.94×10^{-1}
2.111×10^3	3.18×10^1	1.39×10^1	-2.40×10^0
2.127×10^3	3.18×10^1	6.00×10^0	-7.72×10^{-1}
2.142×10^3	3.18×10^1	8.00×10^0	-8.85×10^{-1}
2.155×10^3	3.18×10^1	1.41×10^1	1.36×10^0
2.177×10^3	3.18×10^1	1.00×10^1	2.64×10^0
2.182×10^3	3.01×10^1	8.96×10^1	1.20×10^{-1}
2.198×10^3	3.07×10^1	1.40×10^2	-5.09×10^{-1}
2.223×10^3	3.18×10^1	1.20×10^1	-1.40×10^{-1}
2.230×10^3	3.18×10^1	9.00×10^0	1.17×10^{-1}
2.241×10^3	3.18×10^1	3.41×10^1	-9.16×10^{-1}
2.257×10^3	3.10×10^1	1.37×10^2	4.21×10^{-1}
2.263×10^3	3.18×10^1	1.00×10^1	-1.17×10^{-1}
2.268×10^3	3.18×10^1	8.00×10^0	1.04×10^{-1}
2.278×10^3	3.16×10^1	3.98×10^2	4.62×10^{-1}
2.283×10^3	3.10×10^1	2.79×10^1	7.64×10^{-1}
2.291×10^3	3.09×10^1	2.18×10^2	-2.36×10^{-1}
2.303×10^3	3.18×10^1	1.70×10^1	-1.00×10^{-1}
2.318×10^3	3.18×10^1	1.00×10^1	-4.83×10^0

TABLE IV. *(Continued.)*

Energy (eV)	Γ_γ (meV)	Γ_n (meV)	Γ_f (meV)
2.334×10^3	3.18×10^1	3.78×10^1	5.53×10^{-1}
2.351×10^3	3.18×10^1	3.85×10^1	1.29×10^{-1}
2.360×10^3	3.18×10^1	1.20×10^1	-1.27×10^{-1}
2.366×10^3	3.05×10^1	2.43×10^2	3.84×10^{-1}
2.373×10^3	3.18×10^1	9.65×10^0	-1.03×10^{-1}
2.386×10^3	3.18×10^1	1.83×10^1	1.34×10^0
2.405×10^3	3.18×10^1	2.50×10^1	-6.17×10^{-2}
2.416×10^3	3.18×10^1	6.84×10^1	5.86×10^{-1}
2.425×10^3	3.18×10^1	5.00×10^0	1.04×10^{-1}
2.434×10^3	3.04×10^1	2.15×10^2	3.00×10^{-1}
2.459×10^3	3.18×10^1	2.63×10^1	-4.30×10^{-1}
2.470×10^3	3.18×10^1	4.89×10^1	-2.10×10^{-1}
2.477×10^3	3.18×10^1	1.00×10^1	-5.15×10^0
2.484×10^3	3.18×10^1	2.14×10^1	3.39×10^{-1}
2.512×10^3	3.18×10^1	1.00×10^1	-1.13×10^{-1}
2.521×10^3	3.38×10^1	1.14×10^2	3.50×10^{-1}
2.531×10^3	3.18×10^1	1.50×10^1	-1.04×10^{-1}
2.538×10^3	3.23×10^1	2.87×10^2	2.10×10^{-1}
2.543×10^3	3.18×10^1	7.00×10^{-1}	9.88×10^{-2}
2.549×10^3	3.26×10^1	8.56×10^1	-6.55×10^{-1}
2.563×10^3	3.18×10^1	7.00×10^{-1}	-1.00×10^{-1}
2.575×10^3	3.64×10^1	4.68×10^1	-4.84×10^{-1}
2.578×10^3	3.18×10^1	1.00×10^1	9.50×10^{-2}
2.595×10^3	3.18×10^1	1.00×10^1	-1.12×10^0
2.602×10^3	3.18×10^1	1.00×10^1	6.67×10^0
2.627×10^3	3.18×10^1	1.50×10^1	-8.15×10^{-2}
2.633×10^3	3.18×10^1	1.00×10^1	9.23×10^{-2}
2.645×10^3	3.16×10^1	4.30×10^2	-4.59×10^0
2.652×10^3	3.18×10^1	3.83×10^1	1.36×10^1
2.670×10^3	3.18×10^1	1.00×10^1	-1.02×10^1
2.698×10^3	3.18×10^1	3.26×10^2	1.20×10^2
2.700×10^3	3.18×10^1	1.50×10^1	7.56×10^1
2.706×10^3	3.18×10^1	1.00×10^1	-1.97×10^1
2.718×10^3	3.18×10^1	4.04×10^1	1.97×10^0
2.729×10^3	3.18×10^1	1.00×10^1	-1.02×10^{-1}
2.739×10^3	3.18×10^1	1.82×10^2	6.71×10^{-1}
2.754×10^3	2.91×10^1	1.14×10^2	8.33×10^0
2.764×10^3	3.18×10^1	1.00×10^1	9.80×10^{-2}
2.817×10^3	3.18×10^1	4.43×10^1	-1.60×10^0
2.844×10^3	3.18×10^1	1.72×10^2	-1.28×10^{-1}
2.858×10^3	3.18×10^1	2.87×10^1	1.52×10^0
2.882×10^3	3.18×10^1	3.20×10^1	-3.50×10^{-1}
2.896×10^3	3.18×10^1	6.39×10^1	1.60×10^{-1}
2.905×10^3	3.18×10^1	1.23×10^2	6.10×10^{-1}
2.924×10^3	3.18×10^1	1.80×10^1	-1.00×10^{-1}
2.938×10^3	3.18×10^1	1.53×10^2	-4.00×10^{-1}
2.969×10^3	3.18×10^1	9.87×10^1	-3.60×10^{-1}
2.980×10^3	3.18×10^1	1.12×10^2	5.00×10^{-2}
2.987×10^3	3.18×10^1	1.09×10^1	-9.60×10^{-1}
2.994×10^3	3.18×10^1	6.12×10^1	3.25×10^{-1}
3.004×10^3	3.18×10^1	8.39×10^1	5.65×10^{-1}
3.018×10^3	3.18×10^1	1.27×10^2	-1.93×10^{-1}
3.029×10^3	3.18×10^1	2.01×10^1	2.17×10^0
3.040×10^3	3.18×10^1	1.00×10^1	-2.32×10^{-1}
3.048×10^3	3.18×10^1	1.00×10^1	3.71×10^{-1}
3.055×10^3	3.18×10^1	4.90×10^1	-5.81×10^0
3.070×10^3	3.18×10^1	1.37×10^1	2.76×10^1

TABLE IV. *(Continued.)*

Energy (eV)	Γ_γ (meV)	Γ_n (meV)	Γ_f (meV)
3.078×10^3	3.18×10^1	1.33×10^2	3.82×10^0
3.088×10^3	3.18×10^1	3.35×10^1	-7.94×10^{-1}
3.092×10^3	3.18×10^1	1.00×10^1	-2.59×10^0
3.106×10^3	3.18×10^1	6.00×10^0	-1.27×10^1
3.113×10^3	3.18×10^1	3.97×10^1	8.34×10^{-1}
3.140×10^3	3.18×10^1	4.00×10^0	-4.21×10^0
3.173×10^3	3.18×10^1	2.39×10^2	1.56×10^0
3.185×10^3	3.18×10^1	8.00×10^0	-3.07×10^{-1}
3.192×10^3	3.18×10^1	3.60×10^2	4.41×10^{-1}
3.209×10^3	3.18×10^1	1.50×10^1	3.18×10^{-1}
3.238×10^3	3.18×10^1	7.40×10^1	-7.59×10^{-1}
3.258×10^3	3.18×10^1	6.00×10^0	-3.11×10^{-1}
3.266×10^3	3.18×10^1	2.60×10^1	1.24×10^{-1}
3.269×10^3	3.18×10^1	1.09×10^2	1.72×10^{-1}
3.291×10^3	3.18×10^1	1.00×10^1	-1.81×10^0
3.305×10^3	3.18×10^1	1.20×10^1	-1.01×10^0
3.317×10^3	3.18×10^1	1.50×10^1	2.99×10^{-1}
3.332×10^3	3.18×10^1	1.48×10^1	-1.65×10^0
3.340×10^3	3.18×10^1	1.40×10^1	2.86×10^0
3.346×10^3	3.18×10^1	5.00×10^0	6.25×10^0
3.360×10^3	3.18×10^1	1.30×10^1	-7.34×10^0
3.382×10^3	3.18×10^1	1.50×10^1	-3.09×10^{-1}
3.382×10^3	3.18×10^1	1.60×10^1	2.74×10^3
3.389×10^3	3.18×10^1	1.50×10^1	3.00×10^{-1}
3.423×10^3	3.18×10^1	3.51×10^1	0.00×10^0
3.440×10^3	3.18×10^1	1.00×10^1	-3.39×10^{-1}
3.458×10^3	3.18×10^1	7.12×10^1	-5.48×10^{-1}
3.466×10^3	3.18×10^1	3.65×10^2	-1.60×10^0
3.487×10^3	3.18×10^1	2.50×10^1	3.47×10^{-1}
3.494×10^3	3.18×10^1	6.59×10^1	-1.22×10^0
3.500×10^3	3.18×10^1	1.00×10^1	6.03×10^{-1}
3.514×10^3	3.18×10^1	1.00×10^1	-5.00×10^{-1}
3.539×10^3	3.18×10^1	1.00×10^1	5.00×10^{-1}
3.555×10^3	3.18×10^1	9.06×10^1	0.00×10^0
3.567×10^3	3.18×10^1	1.79×10^2	-2.56×10^{-1}
3.581×10^3	3.18×10^1	1.50×10^1	0.00×10^0
3.595×10^3	3.18×10^1	4.22×10^1	-3.00×10^{-1}
3.610×10^3	3.18×10^1	7.57×10^1	3.02×10^{-1}
3.614×10^3	3.18×10^1	3.80×10^1	3.65×10^{-1}
3.648×10^3	3.18×10^1	1.00×10^1	2.80×10^{-1}
3.657×10^3	3.18×10^1	2.74×10^2	-7.98×10^{-2}
3.665×10^3	3.18×10^1	5.41×10^1	2.83×10^{-1}
3.682×10^3	3.18×10^1	1.00×10^1	-9.01×10^{-1}
3.702×10^3	3.18×10^1	5.37×10^1	9.13×10^{-1}
3.711×10^3	3.18×10^1	2.50×10^1	-5.00×10^{-1}
3.723×10^3	3.18×10^1	5.58×10^1	9.40×10^{-1}
3.743×10^3	3.18×10^1	8.00×10^0	5.00×10^{-1}
3.765×10^3	3.18×10^1	5.00×10^0	-5.00×10^{-1}
3.777×10^3	3.18×10^1	5.00×10^0	-3.25×10^0
3.800×10^3	3.18×10^1	1.08×10^2	1.14×10^0
3.823×10^3	3.18×10^1	8.00×10^0	-4.76×10^{-1}
3.833×10^3	3.18×10^1	4.00×10^0	-4.84×10^{-1}
3.844×10^3	3.18×10^1	8.03×10^1	-9.97×10^{-2}
3.853×10^3	3.18×10^1	1.03×10^2	3.95×10^{-1}
3.859×10^3	3.18×10^1	1.00×10^1	2.70×10^0
3.872×10^3	3.18×10^1	4.51×10^1	1.34×10^0
3.886×10^3	3.18×10^1	1.00×10^1	-5.00×10^{-1}

TABLE IV. *(Continued.)*

Energy (eV)	Γ_γ (meV)	Γ_n (meV)	Γ_f (meV)
3.901×10^3	3.18×10^1	2.30×10^2	1.10×10^{-1}
3.916×10^3	3.18×10^1	1.83×10^2	-2.85×10^{-1}
3.939×10^3	3.18×10^1	1.00×10^1	9.34×10^{-1}
3.954×10^3	3.18×10^1	1.09×10^2	-9.12×10^0
3.960×10^3	3.18×10^1	1.00×10^1	1.00×10^0
3.975×10^3	3.18×10^1	1.19×10^2	-1.36×10^0
3.990×10^3	3.18×10^1	2.90×10^1	9.02×10^{-2}
4.002×10^3	3.18×10^1	2.50×10^1	-9.96×10^0
4.022×10^3	3.18×10^1	3.55×10^2	1.11×10^0
4.031×10^3	3.18×10^1	1.13×10^2	-4.00×10^{-1}
4.055×10^3	3.18×10^1	2.90×10^1	3.00×10^{-1}
4.073×10^3	3.18×10^1	7.50×10^0	3.00×10^{-1}
4.084×10^3	3.18×10^1	1.35×10^2	-3.10×10^{-1}
4.100×10^3	3.18×10^1	2.90×10^2	4.69×10^{-1}
4.110×10^3	3.18×10^1	9.00×10^0	3.00×10^{-1}
4.122×10^3	3.18×10^1	5.42×10^2	1.57×10^{-1}
4.135×10^3	3.18×10^1	6.79×10^1	-3.13×10^{-1}
4.143×10^3	3.18×10^1	5.00×10^0	-3.00×10^{-1}
4.149×10^3	3.18×10^1	2.91×10^2	-2.25×10^{-1}
4.160×10^3	3.18×10^1	9.03×10^1	1.40×10^{-1}
4.170×10^3	3.18×10^1	2.40×10^1	3.00×10^{-1}
4.203×10^3	3.18×10^1	4.61×10^2	-3.31×10^{-1}
4.221×10^3	3.18×10^1	6.89×10^1	5.84×10^{-1}
4.241×10^3	3.18×10^1	6.00×10^0	-5.80×10^0
4.260×10^3	3.18×10^1	8.00×10^0	7.84×10^0
4.271×10^3	3.18×10^1	1.59×10^2	1.93×10^{-1}
4.280×10^3	3.18×10^1	3.10×10^1	-3.00×10^{-1}
4.288×10^3	3.18×10^1	3.23×10^2	1.52×10^{-1}
4.315×10^3	3.18×10^1	3.50×10^1	-2.98×10^{-1}
4.329×10^3	3.18×10^1	3.19×10^2	-3.96×10^{-2}
4.338×10^3	3.18×10^1	7.50×10^0	3.00×10^{-1}
4.363×10^3	3.18×10^1	2.00×10^1	5.86×10^{-1}
4.376×10^3	3.18×10^1	8.20×10^1	0.00×10^0
4.386×10^3	3.18×10^1	3.20×10^1	-6.36×10^{-1}
4.398×10^3	3.18×10^1	7.80×10^1	-1.04×10^0
4.415×10^3	3.18×10^1	5.00×10^1	1.30×10^1
4.422×10^3	3.18×10^1	6.10×10^1	3.07×10^{-1}
4.433×10^3	3.18×10^1	4.70×10^1	3.05×10^0
4.447×10^3	3.18×10^1	1.80×10^1	-3.60×10^{-1}
4.459×10^3	3.18×10^1	1.03×10^2	6.74×10^{-1}
4.473×10^3	3.18×10^1	2.50×10^1	-3.00×10^{-1}
4.491×10^3	3.18×10^1	2.00×10^1	-3.00×10^{-1}
4.502×10^3	3.18×10^1	2.00×10^1	3.00×10^{-1}
4.517×10^3	3.18×10^1	1.00×10^1	-1.88×10^0
4.538×10^3	3.18×10^1	2.60×10^1	3.00×10^{-1}
4.560×10^3	3.18×10^1	2.00×10^1	3.00×10^{-1}
4.570×10^3	3.18×10^1	2.35×10^2	-3.60×10^{-1}
4.588×10^3	3.18×10^1	5.50×10^2	-3.09×10^{-1}
4.599×10^3	3.18×10^1	7.54×10^1	-5.61×10^{-1}
4.615×10^3	3.18×10^1	2.65×10^2	-4.36×10^0
4.646×10^3	3.18×10^1	1.52×10^2	2.24×10^0
4.664×10^3	3.18×10^1	8.00×10^0	-3.00×10^{-1}
4.687×10^3	3.18×10^1	2.00×10^1	3.40×10^0
4.713×10^3	3.18×10^1	5.60×10^1	4.71×10^{-1}
4.721×10^3	3.18×10^1	5.10×10^2	-9.75×10^{-2}
4.745×10^3	3.18×10^1	2.53×10^2	3.01×10^{-1}
4.755×10^3	3.18×10^1	5.47×10^1	-1.66×10^0

TABLE IV. *(Continued.)*

Energy (eV)	Γ_γ (meV)	Γ_n (meV)	Γ_f (meV)
4.769×10^3	3.18×10^1	3.73×10^1	1.33×10^0
4.778×10^3	3.18×10^1	3.42×10^1	6.78×10^{-1}
4.791×10^3	3.18×10^1	1.37×10^2	9.32×10^{-1}
4.800×10^3	3.18×10^1	2.00×10^1	-4.11×10^{-1}
4.812×10^3	3.18×10^1	1.81×10^2	2.83×10^{-1}
4.822×10^3	3.18×10^1	6.34×10^1	5.58×10^0
4.843×10^3	3.18×10^1	1.80×10^1	7.76×10^{-1}
4.868×10^3	3.18×10^1	1.30×10^1	-1.40×10^0
4.894×10^3	3.18×10^1	6.28×10^1	-9.19×10^{-1}
4.912×10^3	3.18×10^1	1.50×10^1	-3.79×10^1
4.933×10^3	3.18×10^1	2.00×10^1	1.90×10^1
4.949×10^3	3.18×10^1	5.17×10^1	-8.26×10^0
4.958×10^3	3.18×10^1	3.20×10^2	4.45×10^0
4.968×10^3	3.18×10^1	1.54×10^2	5.92×10^0
4.974×10^3	3.18×10^1	7.50×10^1	-3.67×10^{-1}
4.994×10^3	3.18×10^1	9.56×10^1	-1.21×10^0
5.035×10^3	3.18×10^1	1.50×10^1	1.47×10^0
5.047×10^3	3.18×10^1	1.00×10^1	-1.51×10^0
5.072×10^3	3.18×10^1	5.66×10^2	-7.53×10^0
5.097×10^3	3.18×10^1	3.60×10^1	2.34×10^0
5.111×10^3	3.18×10^1	8.61×10^1	1.59×10^1
5.120×10^3	3.18×10^1	1.95×10^1	-4.45×10^{-1}
5.131×10^3	3.18×10^1	4.36×10^1	-4.91×10^1
5.148×10^3	3.18×10^1	5.00×10^1	0.00×10^0
5.161×10^3	3.18×10^1	4.00×10^1	1.34×10^0
5.176×10^3	3.18×10^1	8.00×10^0	-2.02×10^0
5.194×10^3	3.18×10^1	3.46×10^2	5.56×10^{-1}
5.216×10^3	3.18×10^1	1.62×10^2	-7.15×10^{-1}
5.235×10^3	3.18×10^1	2.40×10^1	6.37×10^0
5.250×10^3	3.18×10^1	5.23×10^2	-5.94×10^0
5.272×10^3	3.18×10^1	1.44×10^2	2.21×10^1
5.286×10^3	3.18×10^1	5.30×10^1	3.98×10^{-1}
5.301×10^3	3.18×10^1	2.83×10^2	3.46×10^0
5.327×10^3	3.18×10^1	1.78×10^2	-1.28×10^1
5.353×10^3	3.18×10^1	1.50×10^2	2.38×10^0
5.357×10^3	3.18×10^1	3.60×10^1	-4.46×10^{-1}
5.367×10^3	3.18×10^1	6.97×10^1	-8.59×10^0
5.380×10^3	3.18×10^1	8.00×10^0	5.99×10^{-1}
5.393×10^3	3.18×10^1	8.46×10^1	1.06×10^0
5.417×10^3	3.18×10^1	2.64×10^2	3.21×10^{-1}
5.440×10^3	3.18×10^1	1.20×10^1	-3.75×10^0
5.456×10^3	3.18×10^1	8.00×10^0	-4.69×10^{-1}
5.465×10^3	3.18×10^1	4.97×10^1	5.49×10^0
5.483×10^3	3.18×10^1	8.87×10^1	-9.14×10^{-1}
5.498×10^3	3.18×10^1	9.92×10^1	5.23×10^{-1}
5.511×10^3	3.18×10^1	3.58×10^2	-4.83×10^{-1}
5.523×10^3	3.18×10^1	1.75×10^2	4.94×10^0
5.531×10^3	3.18×10^1	1.60×10^1	-5.52×10^{-1}
5.545×10^3	3.18×10^1	5.51×10^2	-3.50×10^{-1}
5.551×10^3	3.18×10^1	1.21×10^2	-7.06×10^{-1}
5.564×10^3	3.18×10^1	1.50×10^1	7.60×10^{-1}
5.574×10^3	3.18×10^1	7.90×10^2	2.26×10^{-1}
5.592×10^3	3.18×10^1	1.96×10^2	7.61×10^{-1}
5.600×10^3	3.18×10^1	1.41×10^2	-3.32×10^{-1}
5.615×10^3	3.18×10^1	6.20×10^1	3.55×10^0

TABLE IV. *(Continued.)*

Energy (eV)	Γ_γ (meV)	Γ_n (meV)	Γ_f (meV)
5.629×10^3	3.18×10^1	2.00×10^1	-6.24×10^{-1}
5.644×10^3	3.18×10^1	5.50×10^1	1.26×10^0
5.667×10^3	3.18×10^1	4.50×10^1	-7.49×10^{-1}
5.682×10^3	3.18×10^1	1.05×10^2	-7.03×10^0
5.692×10^3	3.18×10^1	9.10×10^1	1.00×10^0
5.995×10^3	3.18×10^1	9.64×10^1	-2.74×10^2
5.924×10^3	3.18×10^1	9.58×10^1	-8.72×10^4
5.981×10^3	3.18×10^1	9.62×10^1	-7.39×10^{-2}
5.990×10^3	3.18×10^1	9.63×10^1	1.70×10^{-2}
6.299×10^3	3.18×10^1	9.88×10^1	-2.38×10^0
6.427×10^3	3.18×10^1	9.98×10^1	8.49×10^{-3}
6.446×10^3	3.18×10^1	9.99×10^1	3.22×10^{-1}
6.513×10^3	3.18×10^1	1.00×10^2	2.58×10^0
6.535×10^3	3.18×10^1	1.01×10^2	7.01×10^0
6.551×10^3	3.18×10^1	1.01×10^2	1.87×10^1
6.568×10^3	3.18×10^1	1.01×10^2	2.85×10^2
7.508×10^3	3.18×10^1	1.08×10^2	2.08×10^2
8.021×10^3	3.18×10^1	1.11×10^2	2.98×10^0
8.064×10^3	3.18×10^1	1.12×10^2	3.13×10^0
8.098×10^3	3.18×10^1	1.12×10^2	1.92×10^4
8.361×10^3	3.18×10^1	1.14×10^2	7.80×10^0
8.472×10^3	3.18×10^1	1.77×10^2	1.60×10^1
8.708×10^3	3.18×10^1	1.16×10^2	1.02×10^2
8.975×10^3	3.18×10^1	1.18×10^2	5.59×10^4
1.002×10^4	3.18×10^1	1.25×10^2	8.64×10^0
1.008×10^4	3.18×10^1	1.25×10^2	2.69×10^2
1.015×10^4	3.18×10^1	1.25×10^2	1.16×10^2
1.096×10^4	3.18×10^1	1.30×10^2	6.89×10^1
1.118×10^4	3.18×10^1	1.32×10^2	3.61×10^2
1.150×10^4	3.18×10^1	1.33×10^2	1.15×10^3
1.166×10^4	3.18×10^1	1.34×10^2	-4.64×10^3
1.215×10^4	3.18×10^1	1.37×10^2	3.87×10^2
1.250×10^4	3.18×10^1	1.39×10^2	-8.21×10^1
1.311×10^4	3.18×10^1	1.42×10^2	-4.84×10^2
1.317×10^4	3.18×10^1	1.43×10^2	-4.90×10^4
1.356×10^4	3.18×10^1	1.45×10^2	1.76×10^3
1.405×10^4	3.18×10^1	1.48×10^2	8.55×10^1
1.450×10^4	3.18×10^1	1.50×10^2	2.39×10^2
1.447×10^4	3.18×10^1	1.50×10^2	3.38×10^2
1.605×10^4	3.18×10^1	1.58×10^2	6.44×10^3
1.643×10^4	3.18×10^1	1.60×10^2	-5.70×10^2
1.748×10^4	3.18×10^1	1.65×10^2	3.87×10^3
1.822×10^4	3.18×10^1	1.68×10^2	-2.32×10^3
1.845×10^4	3.18×10^1	1.69×10^2	6.22×10^2
1.921×10^4	3.18×10^1	1.73×10^2	-1.44×10^3

APPENDIX B: CROSS SECTION IN THE 100 KEV–6 MEV REGION

The derived ^{240}Pu(n, f) cross section (σ) along with its corresponding uncertainty $(\delta\sigma)$ is reported in Table V, in the energy region between 100 keV and 6 MeV.

TABLE V. Point-wise ^{240}Pu(n, f) cross section above 100 keV along with the total estimated uncertainties.

Energy (eV)	σ (b)	$\delta\sigma$ (b)	$\delta\sigma$ (%)
1.01×10^5	4.90×10^{-2}	5×10^{-3}	10
1.04×10^5	4.89×10^{-2}	5×10^{-3}	9
1.06×10^5	5.80×10^{-2}	4×10^{-3}	8
1.08×10^5	6.56×10^{-2}	5×10^{-3}	7
1.11×10^5	6.88×10^{-2}	5×10^{-3}	7
1.14×10^5	6.91×10^{-2}	5×10^{-3}	7
1.16×10^5	6.97×10^{-2}	5×10^{-3}	7
1.19×10^5	4.70×10^{-2}	4×10^{-3}	9
1.22×10^5	5.29×10^{-2}	4×10^{-3}	8
1.24×10^5	6.19×10^{-2}	4×10^{-3}	7
1.27×10^5	6.95×10^{-2}	4×10^{-3}	6
1.30×10^5	7.70×10^{-2}	4×10^{-3}	6
1.33×10^5	8.47×10^{-2}	5×10^{-3}	6
1.36×10^5	9.09×10^{-2}	6×10^{-3}	7
1.40×10^5	8.74×10^{-2}	7×10^{-3}	8
1.43×10^5	6.74×10^{-2}	7×10^{-3}	10
1.46×10^5	7.08×10^{-2}	7×10^{-3}	10
1.50×10^5	6.19×10^{-2}	6×10^{-3}	10
1.53×10^5	5.54×10^{-2}	5×10^{-3}	10
1.57×10^5	6.04×10^{-2}	6×10^{-3}	10
1.60×10^5	6.87×10^{-2}	6×10^{-3}	8
1.64×10^5	5.71×10^{-2}	5×10^{-3}	8
1.68×10^5	7.80×10^{-2}	5×10^{-3}	6
1.72×10^5	6.48×10^{-2}	4×10^{-3}	7
1.76×10^5	6.58×10^{-2}	4×10^{-3}	7
1.80×10^5	6.43×10^{-2}	4×10^{-3}	7
1.84×10^5	6.42×10^{-2}	4×10^{-3}	7
1.88×10^5	8.12×10^{-2}	5×10^{-3}	6
1.93×10^5	8.12×10^{-2}	5×10^{-3}	7
1.97×10^5	9.02×10^{-2}	6×10^{-3}	7
2.02×10^5	8.81×10^{-2}	6×10^{-3}	7
2.07×10^5	7.75×10^{-2}	5×10^{-3}	7
2.11×10^5	8.00×10^{-2}	5×10^{-3}	7
2.16×10^5	7.92×10^{-2}	5×10^{-3}	6
2.21×10^5	9.67×10^{-2}	5×10^{-3}	5
2.26×10^5	8.64×10^{-2}	5×10^{-3}	6
2.32×10^5	9.47×10^{-2}	5×10^{-3}	5
2.37×10^5	8.84×10^{-2}	5×10^{-3}	5
2.43×10^5	8.99×10^{-2}	5×10^{-3}	5
2.48×10^5	8.44×10^{-2}	4×10^{-3}	5
2.54×10^5	8.31×10^{-2}	4×10^{-3}	5
2.60×10^5	6.46×10^{-2}	4×10^{-3}	6
2.66×10^5	7.65×10^{-2}	4×10^{-3}	5
2.72×10^5	1.01×10^{-1}	5×10^{-3}	5
2.79×10^5	1.31×10^{-1}	6×10^{-3}	5
2.85×10^5	1.11×10^{-1}	6×10^{-3}	5
2.92×10^5	9.86×10^{-2}	5×10^{-3}	5
2.99×10^5	7.95×10^{-2}	4×10^{-3}	5
3.06×10^5	7.47×10^{-2}	4×10^{-3}	5
3.13×10^5	6.80×10^{-2}	4×10^{-3}	6
3.20×10^5	8.64×10^{-2}	4×10^{-3}	5
3.27×10^5	8.93×10^{-2}	4×10^{-3}	5
3.35×10^5	1.33×10^{-1}	6×10^{-3}	4
3.43×10^5	1.46×10^{-1}	6×10^{-3}	4
3.51×10^5	1.68×10^{-1}	7×10^{-3}	4

TABLE V. *(Continued.)*

Energy (eV)	σ (b)	$\delta\sigma$ (b)	$\delta\sigma$ (%)
3.59×10^5	1.59×10^{-1}	6×10^{-3}	4
3.67×10^5	1.37×10^{-1}	5×10^{-3}	4
3.76×10^5	1.49×10^{-1}	5×10^{-3}	4
3.85×10^5	1.70×10^{-1}	5×10^{-3}	3
3.94×10^5	1.77×10^{-1}	6×10^{-3}	3
4.03×10^5	2.14×10^{-1}	7×10^{-3}	3
4.12×10^5	2.15×10^{-1}	7×10^{-3}	3
4.22×10^5	2.37×10^{-1}	8×10^{-3}	3
4.32×10^5	2.52×10^{-1}	8×10^{-3}	3
4.42×10^5	3.12×10^{-1}	9×10^{-3}	3
4.52×10^5	3.11×10^{-1}	8×10^{-3}	3
4.62×10^5	3.15×10^{-1}	8×10^{-3}	2
4.73×10^5	2.97×10^{-1}	7×10^{-3}	2
4.84×10^5	3.44×10^{-1}	8×10^{-3}	2
4.95×10^5	3.31×10^{-1}	7×10^{-3}	2
5.07×10^5	3.62×10^{-1}	7×10^{-3}	2
5.19×10^5	4.17×10^{-1}	8×10^{-3}	2
5.31×10^5	4.68×10^{-1}	9×10^{-3}	2
5.43×10^5	4.97×10^{-1}	1×10^{-2}	2
5.56×10^5	5.45×10^{-1}	1×10^{-2}	2
5.69×10^5	5.67×10^{-1}	1×10^{-2}	2
5.82×10^5	6.49×10^{-1}	1×10^{-2}	2
5.96×10^5	6.78×10^{-1}	1×10^{-2}	2
6.10×10^5	7.41×10^{-1}	1×10^{-2}	2
6.24×10^5	7.32×10^{-1}	1×10^{-2}	2
6.38×10^5	7.75×10^{-1}	1×10^{-2}	2
6.53×10^5	8.35×10^{-1}	1×10^{-2}	2
6.68×10^5	7.94×10^{-1}	1×10^{-2}	2
6.84×10^5	8.31×10^{-1}	1×10^{-2}	2
7.00×10^5	8.62×10^{-1}	1×10^{-2}	2
7.16×10^5	8.97×10^{-1}	2×10^{-2}	2
7.33×10^5	9.23×10^{-1}	2×10^{-2}	2
7.50×10^5	9.74×10^{-1}	2×10^{-2}	2
7.67×10^5	1.05×10^0	2×10^{-2}	2
7.85×10^5	1.04×10^0	2×10^{-2}	2
8.04×10^5	1.03×10^0	2×10^{-2}	2
8.22×10^5	1.11×10^0	2×10^{-2}	2
8.41×10^5	1.17×10^0	2×10^{-2}	2
8.61×10^5	1.20×10^0	2×10^{-2}	2
8.81×10^5	1.22×10^0	2×10^{-2}	1
9.02×10^5	1.28×10^0	2×10^{-2}	1
9.23×10^5	1.32×10^0	2×10^{-2}	1
9.44×10^5	1.38×10^0	2×10^{-2}	1
9.66×10^5	1.43×10^0	2×10^{-2}	1
9.89×10^5	1.47×10^0	2×10^{-2}	1
1.05×10^6	1.48×10^0	1×10^{-2}	1
1.15×10^6	1.51×10^0	1×10^{-2}	1
1.25×10^6	1.49×10^0	1×10^{-2}	1
1.35×10^6	1.49×10^0	1×10^{-2}	1
1.45×10^6	1.57×10^0	2×10^{-2}	1
1.55×10^6	1.56×10^0	2×10^{-2}	1
1.65×10^6	1.58×10^0	2×10^{-2}	1
1.75×10^6	1.60×10^0	2×10^{-2}	1
1.85×10^6	1.66×10^0	2×10^{-2}	1
1.95×10^6	1.65×10^0	2×10^{-2}	1
2.10×10^6	1.71×10^0	2×10^{-2}	1

TABLE V. *(Continued.)*

Energy (eV)	σ (b)	$\delta\sigma$ (b)	$\delta\sigma$ (%)
2.30×10^6	1.70×10^0	2×10^{-2}	1
2.50×10^6	1.60×10^0	3×10^{-2}	2
2.70×10^6	1.72×10^0	3×10^{-2}	2
2.90×10^6	1.73×10^0	3×10^{-2}	2
3.12×10^6	1.71×10^0	4×10^{-2}	2
3.38×10^6	1.71×10^0	4×10^{-2}	2

TABLE V. *(Continued.)*

Energy (eV)	σ (b)	$\delta\sigma$ (b)	$\delta\sigma$ (%)
3.62×10^6	1.61×10^0	4×10^{-2}	2
3.88×10^6	1.64×10^0	8×10^{-2}	5
4.25×10^6	1.52×10^0	8×10^{-2}	5
4.75×10^6	1.55×10^0	8×10^{-2}	5
5.25×10^6	1.52×10^0	8×10^{-2}	5
5.75×10^6	1.63×10^0	1×10^{-1}	8

[1] IAEA, Energy, Electricity and Nuclear Power Estimates for the Period up to 2050, Technical Report No. IAEA-RDS1-2017, 2017.

[2] Generation-IV International Forum, www.gen-4.org/gif/

[3] F. Goldner and R. Versluis, Transmutation capabilities of generation 4 reactors, NEA Technical Report No. OECD-NEA-39088792, 2007.

[4] NEA, Technical Report, 2002, www.oecd-nea.org/ndd/reports/2002/nea3109.html

[5] A. Stanculescu, Ann. Nucl. Energy **62**, 607 (2013).

[6] S. Gabriel, A. Baschwitz, G. Mathonnière, F. Fizaine, and T. Eleouet, Resour. Policy **38**, 458 (2013).

[7] The Nuclear Energy Agency (NEA), www.oecd-nea.org/

[8] The High Priority Request List (HPRL), www.oecd-nea.org/dbdata/hprl/

[9] High priority request ID 37, www.oecd-nea.org/dbdata/hprl/hprlview.pl?id=457, 2008.

[10] M. Salvatores, International Evaluation Co-operation: Uncertainty and Target Accuracy Assessment for Innovative Systems Using Recent Covariance Data Evaluations, NEA-OECD Technical Report, 2008.

[11] Plutonium management in the medium term, White Paper on the Physics of Plutonium Fuels and I. F. C. 1070 (WPPR), OECD-NEA Technical Report, 2002.

[12] N. Otuka *et al.*, Nucl. Data Sheets **120**, 272 (2014).

[13] W. W. Pratt *et al.*, Oak Ridge National Laboratory Progress Report 2081, 1956.

[14] T. A. Eastwood, in *Proceedings of the 2nd International Conference on the Peaceful Uses of Atomic Energy*, Geneva, Switzerland (International Atomic Energy Agency, Vienna, 1958), Vol 16, p. 53.

[15] C. B. Bigham, Can. J. Phys. **36**, 503 (1958).

[16] E. K. Hulet, H. R. Bowman, M. C. Michel, and R. W. Hoff, Phys. Rev. **102**, 1621 (1956).

[17] B. Leonard, Jr. *et al.*, Bull. Am. Phys. Soc. **1**, 248 (1956).

[18] L. W. Weston and J. H. Todd, Nucl. Sci. Eng. **88**, 567 (1984).

[19] O. Bouland *et al.*, Nucl. Sci. Eng. **127**, 105 (1997).

[20] C. Budtz-Jorgensen and H. H. Knitter, Nucl. Sci. Eng. **79**, 380 (1981).

[21] P. Salvador-Castineira *et al.*, Phys. Rev. C **92**, 014620 (2015).

[22] F. Tovesson, T. S. Hill, M. Mocko, J. D. Baker, and C. A. McGrath, Phys. Rev. C **79**, 014613 (2009).

[23] A. B. Laptev *et al.*, Nucl. Phys. A **734**, E45 (2004).

[24] A. Tsinganis *et al.*, *Fission cross section measurements for* ^{240}Pu, ^{242}Pu*: Deliverable 1.5 of the ANDES project* (Publications Office of the European Union, Belgium 2013).

[25] C. Weiss *et al.*, Nucl. Instrum. Methods A **799**, 90 (2015).

[26] A. Tsinganis, A. Stamatopoulos *et al.*, in *Proceedings of the 14th International Conference on Nuclear Reaction Mechanisms*, edited by F. Cerutti, M. Chadwick, A. Ferrari, T. Kawano, and P. Schoofs (CERN, Geneva, 2015).

[27] A. Stamatopoulos *et al.*, EPJ Web Conf. **146**, 04030 (2017).

[28] M. Barbagallo *et al.*, Phys. Rev. Lett. **117**, 152701 (2016).

[29] A. Stamatopoulos *et al.*, in ND2019 Proceedings [EPJ Web Conf. (to be published)].

[30] V. Michalopoulou *et al.*, in ND2019 Proceedings [EPJ Web Conf. (to be published)].

[31] Z. Eleme *et al.*, in ND2019 Proceedings [EPJ Web Conf. (to be published)].

[32] M. Sabate-Gilarte *et al.*, Eur. Phys. J. A **53**, 210 (2017).

[33] G. Sibbens *et al.*, J. Radiol. Nucl. Chem. **299**, 1093 (2014).

[34] A. Stamatopoulos, Study of the ^{240}Pu(n, f) and ^{237}Np(n, f) reaction cross sections at the new experimental area (EAR2) of the CERN n_TOF facility, Doctoral thesis, Report No. CERN-THESIS-2019-260, National Technical University of Athens, 2019.

[35] S. Andriamonje *et al.*, J. Instrum. **5**, P02001 (2010).

[36] L. Cosentino *et al.*, Rev. Sci. Instrum. **86**, 073509 (2015).

[37] U. Abbondanno *et al.*, Nucl. Instrum. Methods A **538**, 692 (2005).

[38] P. Žugec *et al.*, Nucl. Instrum. Methods A **812**, 134 (2016).

[39] M. Robles, Study of fast radiation-detectors based on fast halide scintillator crystals and their application to the CERN n_TOF experiment, Doctoral thesis, Report No. CERN-THESIS-2016-399, University of Santiago de Compostela, 2016.

[40] K.-H. Schmidt *et al.*, General fescription of fission observables: GEF model, OECD Technical Report No. NEA/DB/DOC 1, 2014.

[41] A. Ferrari *et al.*, FLUKA: A multi-particle transport code, CERN Technical Report No. INFN/TC_05/11, CERN-2005-10, 2005.

[42] G. Sibbens *et al.*, in *Proceedings of the 28th World Conference of the International International Target Development Society (INTDS2016)*, 13–18 November 2016, Stellenbosch, South Africa, edited by N. Kheswa and J. Greene, AIP Conf. Proc. No. 1962 (AIP, New York, 2018), p. 030007.

[43] P. B. Coates, J. Phys. E **5**, 148 (1972).

[44] M. Moore, Nucl. Instrum. Methods **169**, 245 (1980).

[45] A. Stamatopoulos *et al.*, Nucl. Instrum. Methods A **913**, 40 (2019).

[46] N. Colonna *et al.*, Eur. Phys. J. A **56**, 48 (2020).

[47] E. Leal-Cidoncha, I. Durán, C. Paradela, D. Tarrío *et al.*, EPJ Web Conf. **111**, 10002 (2016).

[48] D. Tarrío, L. Leong, L. Audouin, I. Duran *et al.*, Nucl. Data Sheets **119**, 35 (2014).

[49] D. Tarrío, L. Leong, L. Audouin, I. Duran *et al.*, Nucl. Instrum. Methods Phys. Res., Sect. A **743**, 79 (2014).

[50] NIST standard reference database 124, 2017.

[51] M. Sabaté Gilarte, The n_TOF-EAR2 facility at CERN: Neutron flux determination and the ^{33}S$(N, \alpha)^{30}$Si cross section measurement; implications in BNCT, Doctoral thesis, Report No. CERN-THESIS-2014-385, CERN, Universidad de Sevilla, 2017.

[52] Z. Ge, H. Wu, G. Chen, and R. Xu, EPJ Web Conf. **146**, 02002 (2017).

[53] JEFF-3.3: Evaluated Data Library, 2017.

[54] D. Brown *et al.*, Nucl. Data Sheets **148**, 1 (2018).

[55] K. Shibata *et al.*, J. Nucl. Sci. Technol. **48**, 1 (2011).

[56] J. W. Meadows, Nucl. Sci. Eng. **79**, 233 (1981).

[57] V. G. Nesterov and G. N. Smirenkin, Sov. J. At. Energy **9**, 511 (1961).

[58] K. Kari, Ph.D. thesis, Kernforschungszentrum Karlsruhe, 1978 (unpublished), Technical Report 2673.

[59] K. Kari and S. Cierjacks, in *Proceedings of the Third Symposium on Neutron Capture Gamma-Ray Spectroscopy and Related Topics* (Plenum Press, New York, 1978).

[60] K. Kari and S. Cierjacks, in *Proceedings of the Specialists Meeting on Nuclear Data of Plutonium and Americium Isotopes for Reactor Applications*, edited by R. E. Chrien (OSTI.GOV, 1978).

[61] M. Cance and G. Grenier, Nuclear Data for Science and Technology, in *Proceedings of the International Conference Antwerp 610 September 1982*, edited by K. H. Böckhof (Springer, 1982).

[62] M. Kazarinova, Yu. S. Zamyatnin, and V. Gorbachev, At. Energiya **9**, 16 (1960).

[63] N. M. Larson, ORNL Technical Report No. ORNL/TM-9179/R8 ENDF-364/R2, 2008.

[64] V. Vlachoudis (private communication).

[65] R. Gwin, EXFOR entry 14249002, 1982.

[66] C. Guerrero, Doctoral thesis, CIEMAT, Madrid, 2008 (unpublished), CERN-THESIS-2010-064.

[67] C. Guerrero *et al.*, in *ANS Topical Meeting on Reactor Physics, PHYSOR-2006* (ANS, La Grange Park, IL, 2006), p. C031.

[68] W. Kolar and K. Böckhoff, J. Nucl. Energy **22**, 299 (1968).